# UNIVERSITE de PARIS-SUD
# U.F.R. SCIENTIFIQUE D'ORSAY

## mémoire d'habilitation
présenté par
Jean-Marc Le Goff

Title: The spin structure of the nucleon

soutenue le lundi 14 février 2005 devant la commission d'examen:

Président:      J. Haissinski
Rapporteurs:    S. Forte
                A. Milsztajn
                A. Staude
Examinateurs:   A. Magnon
                J. Soffer

# Contents

# Remerciements

J. Haissinski a bien voulu présider le jury de cette habilitation. Je l'en remercie très sincèrement ainsi que S. Forte, A. Milsztajn, et A. Staude qui ont accepté d'en être les rapporteurs, et A. Magnon et J. Soffer qui sont également membres du jury.

Je tiens aussi à remercier vivement P.J. Carlos qui m'a embauché au Service de Physique Nucléaire (SPhN) du CEA ainsi que ces successeurs J. Mougey, J. Martino et N. Alamanos.

Je ne saurai trop remercier A. Magnon qui après m'avoir convaincu de le rejoindre au sein de la collaboration SMC m'a guidé dans mes choix et m'a toujours apporté un soutien sans faille.

Le travail expérimental est un travail d'équipe et je dois bien sur beaucoup aux autres membres de l'équipe Saclay au sein des collaborations SMC puis COMPASS, J. ball, G. Bardin, Y. Bedfer, C. Bernet, N. de Botton, E. Burtin, C. Cavata, N. D'Hose, J.C. Faivre, F. Feinstein, B. Frois, F. Kunne, F. Lehar, A. de Lesquen, C. Marchand, F. Marie, J. Marroncle, J. Martino, D. Neyret, S. Panebianco, H. Pereira, S. Platchkov, S. Procureur, T. Pussieux, M. Seimetz, D. Thers, E. Tomasi et J. Zhao.

Je ne peux pas citer tout les membres de ces deux collaborations avec lesquels j'ai eu la chance de travailler mais je voudrais quand même mentionner J. Pretz, E. Rondio et R. Windmolders avec qui j'ai travaillé très étroitement et avec le plus grand plaisir ainsi que M. Litmaath dont l'aide a toujours été très précieuse.

Durant ces années j'ai eu l'occasion de m'entretenir avec de nombreux théoriciens qui m'ont aidé à mieux comprendre les subtilités de la structure en spin du nucléon, en particulier I. Bojak, S. Forte, P. Guichon, J. Soffer, M. Stratman et W. Vogelsang ainsi que B. Pire avec lequel j'ai eu de plus le plaisir de partager un enseignement. Qu'ils trouvent tous ici l'expression de ma profonde gratitude.

Dans le cadre de l'expérience SMC j'ai bénéficié de l'aide des services techniques de Saclay, en particulier de la part de R. Azoulay, C. Curé, J.F. Gournay, J.C. Languillat et G. Matichard.

Je remercie les différentes secrètaires du service pour leur aide et leur disponibilité, en particulier D. Coret et I. Richard, ainsi que Lynn Veronneau dont l'aide m'a été si précieuse quand j'étais contactman de la collaboration SMC et qu'elle en était la secrétaire.

Ce mémoire d'habilitation a été reproduit et relié par les soins de V. Poyeton à qui j'exprime mes plus vifs remerciements.

# Introductory remarks

Since the end of my PhD thesis in November 1991, I worked mainly on the study of the spin of the nucleon, in the SMC and in the COMPASS collaborations. However, just after my PhD, I spent some time doing pre-studies for a Møller and a Compton polarimeter for JLab and writing a proposal in the framework of the ELFE project. I also taught hadronic physics at the DEA *Champs Particules Matière* in Orsay for five years.

This report is restricted to my main activity. It includes a pedagogical introduction of some 60 pages to the topic of the spin of the nucleon and to the activities of the SMC and COMPASS collaborations. Since it is supposed to be a pedagogical text it includes only a limited set of references, but it refers to several reviews which include many more references. The text was finished in spring 2004 and the last pages present a status of the field at this time. They were not updated after the several months of administrative delay before the defense of the *habilitation*.

This introductory text is accompanied by several publications, proceedings or internal notes which are particularly related to my personal contributions, namely :

- Publications :

  - Phys. Rev. D56 (1997) 5330. Detailed description of the SMC experiment. I had an important contribution to the sections describing the theory and the analysis.
  - Phys. Lett. B420 (1998) 180. Description of the semi-inclusive analysis of SMC data, which I coordinated.

- Proceedings describing work which I performed :

  - NIM A356 (1995) 96. Description of SMC Polarized Target control.
  - Nucl. Phys. A711 (2002) 56c. An estimate of COMPASS possibilities in terms of transversity with the SMC PT magnet of limited acceptance.

- Internal notes (work performed essentially by me, with the exception of the alignment which I supervised.)

  - SMC 1996-09. Describes how to apply correctly radiative corrections to the SMC data.
  - COMPASS 2000-13. An analytical determination, event by event, of the $D^0$ mass resolution.

- COMPASS 2002-2. An evaluation of the open charm channel in COMPASS.

- COMPASS 2003-4. The COMPASS detector alignment procedure.

- COMPASS 2004-3. Weighted method for asymmetry extraction.

- COMPASS 2004-4. Semi-inclusive correlations (work performed at the SMC time but released as a note only for the analysis of COMPASS data).

# Chapter 1

# Introduction

The atomic nucleus is made of protons and neutrons, which we call *nucleons* since they are the constituents of the nucleus. Nucleons themselves have a structure: they are made of *quarks*. The role of *hadronic* physics is to understand the structure of these nucleons and more generally of the large spectrum of other particles made of quarks and which are generically called *hadrons*.

A large part of our understanding of the hadron structure arises from the *Quark Model* (QM) which provides a good description of the hadron spectrum and for instance predictions for their magnetic moments [1]. The QM is a model in terms of *constituent quarks*, which are effective degrees of freedom. These constituent quarks have a structure, their mass is about one third of the nucleon mass and they carry the hadron quantum numbers.

Our knowledge of the hadron structure also relies on a gauge theory of the strong interaction, called the *Quantum Chromodynamics* (QCD). The quarks of QCD are fundamental degrees of freedom, pointlike and structureless and they interact through the exchange of *gluons*. Three flavors of quarks, up (u), down (d) and strange (s), have a low mass compared to the nucleon and contribute significantly to its structure. The contribution from the three heavy quarks flavors, charm (c), bottom (b) and top (t), is essentially negligible.

However, the perturbative approach used to solve QCD equations can only be applied at high energy, where the coupling constant is small. At low energy it is of the order of unity, so we cannot compute the hadron structure from QCD. In these conditions, the QM, even being just a model, remains very relevant and understanding the relationship between the QM and QCD is of great importance. In this framework we will see that the issue of the spin of the nucleon appears particularly interesting.

The nucleon is a spin 1/2 particle. This spin can be decomposed into the contributions of its constituents :

$$\frac{1}{2} = \frac{1}{2}\Delta\Sigma + \Delta g + L_q + L_g. \tag{1.1}$$

5

Here, $\Delta\Sigma$ is the total number of quarks with spin parallel to the spin of the nucleon minus the number of quarks with spin anti-parallel; once weighted by the spin of the quark, i.e. $1/2$, this is the contribution from the spin of the quarks to the nucleon spin. Similarly, $\Delta g$ is the contribution from the spin of the gluons (which have spin 1). Finally, $L_q$ and $L_g$ are the contributions from the orbital momentum of quarks and gluons, respectively.

In its simplest configuration, the nucleon is made of 3 valence quarks, 2 with spin parallel to the spin of the nucleon and one with spin anti-parallel, $1/2 + 1/2 - 1/2 = 1/2$. In this case $\Delta\Sigma = 1$ and all other contributions are zero. We can also have 3 quarks with spin parallel and a gluon with spin anti-parallel, $1/2 + 1/2 + 1/2 - 1 = 1/2$, in which case $\Delta\Sigma = 3$ and $\Delta g = -1$, or configurations with $q\bar{q}$ pairs (sea quarks), or with non-zero orbital momentum contributions, ...  Finally, when we average over all the configurations, taking into account their probability, the different contributions can a priori assume any real value.

What can QM and QCD say about the spin of the nucleon ?  The most simple, non relativistic, version of the QM corresponds to the simplest configuration above, with $\Delta\Sigma = 1$ and $\Delta g = L_q = L_g = 0$. Including relativistic corrections gives $\Delta\Sigma \approx 0.75$, $L_q \approx 0.125$ and $\Delta g = L_g = 0$ [1]. Due to all the successes of the QM, this prediction is expected to be, at least qualitatively, valid. We are not able to compute $\Delta\Sigma$ within QCD since this is a low energy, non-perturbative quantity. However, it can be decomposed into the contributions from the various quark flavors, $\Delta\Sigma = \Delta u + \Delta d + \Delta s$. Assuming $\Delta s = 0$, which seems reasonable since it is known that the strange flavor contribution to the nucleon structure is generally small, and using the hyperons $\beta$ decay constants in the framework of $SU(3)$ *flavor symmetry*, it was shown that $\Delta\Sigma \approx 0.6$ (see section 2.2.5).

The contributions to the spin of the nucleon, from QCD quarks and constituent quarks, seemed to be quite compatible and it was considered that we had a fair understanding of the question.  The results of the EMC experiment [2] in 1988 then came as a big surprise. This experiment had measured spin asymmetries in high energy muon proton *deep inelastic scattering* and from the extracted spin *structure function* $g_1^p(x)$ inferred a contribution from QCD quarks, $\Delta\Sigma = 0.12 \pm 0.09 \pm 0.14$ and $\Delta s = -0.19 \pm 0.03 \pm 0.04$. This result was often advertised at this time as the "spin crisis" and triggered a very strong activity both on the experimental and the theoretical side. This is illustrated by the fact that the EMC paper appears in the SLAC-SPIRES database [3] with more than 1000 citations, i.e. as the third experimental paper ever, just after the neutrino oscillations at SuperKamiokande and the $J/\psi$ discovery.

After a pedagogical introduction to the problem of the spin of the nucleon, this report will focus on the SMC and COMPASS experiments. SMC aimed at checking and improving the EMC result. SMC also performed a measurement on the deuterium in order to test, for the first time, the *Bjorken sum rule*, which is a fundamental prediction of QCD. The COMPASS experiment was approved in 1997 and started collecting data in 2002. Its main objectives are the gluon polarization, $\Delta g/g$, and the so-called *transversity*.

# Chapter 2

# The spin structure of the nucleon

The spin structure of the nucleon, and in particular the contribution, $\Delta\Sigma$, of the spin of the quarks to the spin of the nucleon can be studied through polarized *deep inelastic scattering* (DIS). We will first introduce DIS and the so-called *parton model* and then turn to the case of polarized DIS in the *inclusive* and *semi-inclusive* cases. Much more details on these topics can be found in review papers [4] or books [5, 6]. We will then discuss how a third *parton distribution*, called *transversity*, appears together with the unpolarized and the longitudinally polarized (or helicity) ones. Finally, we will discuss how the (longitudinally) polarized gluon distribution can be measured.

## 2.1 Deep inelastic scattering (DIS)

Deep inelastic scattering (DIS) refers to the scattering of a high energy lepton, $k_\mu = (E, 0, 0, E)$, off a nucleon, $P_\mu = (M, 0, 0, 0)$, as $k+P \to k'+X$. In the one photon exchange approximation (Fig. 2.1), the scattering occurs via the exchange of a virtual photon, $q_\mu = k_\mu - k'_\mu$. The exchange of 2 photons is neglected; it is suppressed by a factor $\alpha = e^2/4\pi \approx 1/137$ [1], which is the electromagnetic coupling constant, also known as the fine structure constant. In *inclusive* DIS only the scattered lepton, $k'_\mu = (E', 0, E'\sin\theta, E'\cos\theta)$, is measured and there are only two independent Lorentz invariants. They can be chosen as $Q^2 = -q_\mu^2$, the invariant mass of the virtual photon, and the Bjorken variable $x_{bj} = Q^2/2Pq$ which we shall later note $x$ for simplicity. The invariant $Q^2$ is the resolution of the electromagnetic probe. As explained in section 2.1.2, in the framework of the *parton model*, $x$ is interpreted as the fraction of the proton momentum carried by the quark which absorbed the virtual photon. From the theoretical point of view, DIS can be defined as the limit $Q^2 \to \infty$ at fixed $x$: we observe point-like objects (only point-like objects can be seen when $Q^2 \to \infty$) which carry a fixed fraction of the nucleon momentum. Other useful kinematic variables are $y = P.q/P.k$, which in the laboratory frame reduces to $y = \nu/E$ with $\nu = E - E'$ the energy transfer, and $W^2 = (P + q)^2$ the invariant mass of

---

[1] actually $\alpha = e^2/4\pi\hbar c$ but we use natural unit for which $\hbar = c = 1$.
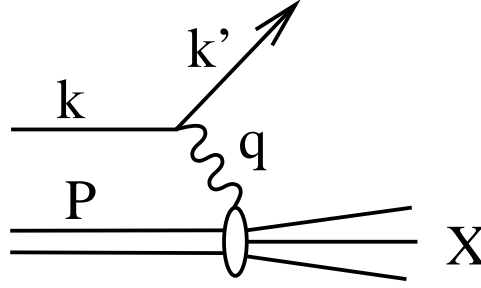
the hadronic residual system X.



Figure 2.1: Deep Inelastic Scattering of a lepton off a nucleon through the exchange of a virtual photon.

## 2.1.1   Cross sections and structure functions

The inclusive DIS cross-section can be written in terms of the *leptonic tensor* $L^{\mu\nu}$ and the *hadronic tensor* $W^{\mu\nu}$ as

$$\frac{d\sigma}{dE'd\Omega} = \frac{\alpha^2}{Q^4}\frac{E'}{E}L^{\mu\nu}W_{\mu\nu}. \tag{2.1}$$

where we have already summed over the final lepton spin, since in practice it is never measured. Since leptons are point-like the expression of the leptonic tensor is known. In the unpolarized case it is: $L^{\mu\nu} = 2[k'_\mu k_\nu + k'_\nu k_\mu + \frac{q^2}{2}g_{\mu\nu}]$, where $g_{\mu\nu}$ is the metric tensor, i.e. a diagonal matrix with $g_{00} = 1$ and $g_{11} = g_{22} = g_{33} = -1$. The expression of $L^{\mu\nu}$ is symmetric in $\mu \leftrightarrow \nu$, whereas in the polarized case an additional antisymmetric term will appear.

The nucleon has a structure so that the hadronic tensor is not known. However, the structure of this tensor has to satisfy some general requirements. The problem involves only two independent Lorentz vectors, e.g. $P_\mu$ and $q_\mu$, so the most general expression for the hadronic tensor is a linear combination of the metric tensor $g_{\mu\nu}$ and of all tensors built from $P_\mu$ and $q_\mu$. The coefficients of this combination must be Lorentz invariants, i.e. functions of $x$ and $Q^2$. Requiring parity, time reversal and translation invariances, hermiticity, and removing antisymmetric terms since they will not contribute after contraction with the symmetric leptonic tensor, the expressions is limited to:

$$W^{\mu\nu} = -W_1 g^{\mu\nu} + W_2\frac{p^\mu p^\nu}{M^2} + W_3\frac{q^\mu q^\nu}{M^2} + W_4\frac{p^\mu q^\nu + p^\nu q^\mu}{M^2},$$

where the $W_i$ are real functions of $x$ and $Q^2$. Current conservation requires $q_\mu W^{\mu\nu} = 0$ and the tensor reduces to :

$$W^{\mu\nu} = W_1\left[-g^{\mu\nu} + \frac{q^\mu q^\nu}{q^2}\right] + W_2\frac{1}{M^2}\left(p^\mu - \frac{pq}{q^2}q^\mu\right)\left(p^\nu - \frac{pq}{q^2}q^\nu\right).$$

The functions $W_1(x, Q^2)$ and $W_2(x, Q^2)$ are called *structure functions*: they are a parametrization of our ignorance of the nucleon structure. They are usually replaced by the dimensionless structure functions $F_1(x, Q^2) = MW_1(x, Q^2)$ and $F_2(x, Q^2) = \nu W_2(x, Q^2)$.

The contraction of $L^{\mu\nu}$ and $W^{\mu\nu}$ gives for the cross section:

$$\frac{d^2\sigma}{dxdQ^2} = \frac{4\pi\alpha^2}{Q^4 x}\left[xy^2 F_1(x, Q^2) + (1 - y - \frac{\gamma^2 y^2}{4})F_2(x, Q^2)\right],\qquad(2.2)$$

where the lepton mass terms are neglected (see e.g. [7] for the full formulas) and $\gamma^2 = Q^2/\nu^2 = 2Mx/\nu \ll 1$. One can also introduce (see section 2.2.2) the ratio $R$ of the longitudinal to the transverse virtual-photon absorption cross-section, $R = \sigma^L/\sigma^T = (1 + \gamma^2)\frac{F_2}{2xF_1} - 1$.

## 2.1.2 The parton model

We consider a reference frame in which the nucleon moves with a very large momentum along $z$, the so-called *infinite momentum frame*. All masses and all quark and gluon momenta transverse to $z$ can be neglected and the nucleon can be considered as a collection of massless constituents, the partons, which move parallel to $z$. In addition, at the time scale of the interaction, $\approx 1/\sqrt{Q^2}$, the fluctuations of the nucleon are frozen; the probe sees free constituents in the nucleon. In this frame the nucleon has a quadri-momentum $P_\mu = (P, 0, 0, P)$. Let us define by $\xi$ the fraction of the nucleon momentum carried by a given parton, which then has a quadri-momentum $p_\mu = (\xi P, 0, 0, \xi P)$. Since the virtual photon is absorbed by a parton: $p + q \to p'$, we have $0 = p'^2 = (p + q)^2 = (\xi P + q)^2 = 0 + 2\xi Pq + q^2$ and $\xi = -q^2/2Pq = x$. So, the Bjorken $x$ variable is the fraction of the proton momentum carried by the parton which absorbed the virtual photon (when momenta are measured in the infinite momentum frame). We have $0 < x < 1$ in agreement with this interpretation [2]. The parton which absorbed the virtual photon has to be a quark and not a gluon since the latter does not carry electromagnetic charge.

One can introduce parton distribution functions (pdf): $f_i(x)$ represents the density probability of finding a parton of flavor $i$ with a fraction $x$ of the nucleon momentum. Since we sum over all final states $X$ the lepton-nucleon cross-section can then be written as an incoherent sum over the lepton-quark cross-sections [3] :

$$\left(\frac{d\sigma}{dxdQ^2}\right)_{lN\to lX} = \sum_i \int_0^1 d\xi f_i(\xi)\left(\frac{d\sigma}{dxdQ^2}\right)_{lq_i\to lq_i},\qquad(2.3)$$

where we sum over the quark flavors and integrate over their momentum. As detailed in Ref. [6] neglecting masses $\left(\frac{d\sigma}{dxdQ^2}\right)_{lq_i\to lq_i} = \frac{2\pi\alpha^2 e_i^2}{Q^4}(y^2 - 2y + 2)\delta(\xi - x)$. Inserting this expression in Eq. (2.3) and performing the integration over $\xi$ gives

$$\left(\frac{d\sigma}{dxdQ^2}\right)_{lN\to lX} = \frac{2\pi\alpha^2}{Q^4}(y^2 - 2y + 2)\sum_i e_i^2 f_i(x).\qquad(2.4)$$

---

[2]For a space-like virtual photon $q^2 < 0$ and $Pq = M\nu > 0$; so $x = -q^2/2Pq > 0$. We have $(q + P)^2 = M_X^2$, so $-Q^2 + 2Pq = M_X^2 - M^2 > 0$, $Q^2 < 2Pq$ and $x < 1$.

[3]This can be justified more rigorously with the optical theorem. For each quark flavor the photo-absorption cross-section is proportional to the imaginary part of the forward Compton amplitude. To get the Compton amplitude for all flavors, one must sum all the Compton amplitudes; then also the corresponding photo-absorption cross-sections have to be summed.

Comparing with Eq. (2.2), where we consistently neglect the mass term $\gamma^2 y^2/4$, leads to $xy^2 F_1(x, Q^2) + (1-y)F_2(x, Q^2) = \frac{1}{2}x(y^2 - 2y + 2)\sum e_i^2 f_i(x)$. This should hold independently of the beam energy, i.e. independently of $y$ at any given $x$ and $Q^2$, so

$$2xF_1(x, Q^2) = F_2(x, Q^2) = \sum_i e_i^2 x f_i(x). \tag{2.5}$$

This relation between $F_1$ and $F_2$, is called the *Calan-Gross* relation. It implies that $R = \sigma^L/\sigma^T = (1+\gamma^2)\frac{F_2}{2xF_1} - 1 \approx 0$ since $\gamma^2 \ll 1$. It was obtained assuming that quarks have spin $\frac{1}{2}$. A different spin would give a different relation. The fact that the relation is experimentally verified proves that quarks indeed have spin $\frac{1}{2}$. Note also that in this relation the structure functions depend only on $x$ and not on the resolution $Q^2$. This means that the lepton scatters on particles which do not involve any scale, i.e. on point-like particles. The fact that the structure functions indeed do not depend on $Q^2$, the so-called *scaling* discovered in 1970 at SLAC [8], was the experimental validation of the parton model. What came as a surprise in this experiment was the fact that this scaling starts to manifest itself at $Q^2 \approx 1$ GeV$^2$.

The quantity $\sum_i \int_0^1 x q_i(x)$ represents the total fraction of the nucleon momentum carried by all quark flavors. Starting from the measured $\int_0^1 (F_2^p + F_2^n)$ and using isospin symmetry (e.g. $u^p = d^n$) it can be shown to be $\approx 1/2$. Quarks alone do not fill the *momentum sum rule*. This means that there are other constituents inside the nucleon without electric charge, these are the gluons of QCD.

The pdf's were introduced in the framework of DIS. It is important to note that they are, however, universal quantities. The same pdf's enter the computation of many processes. For instance the Drell-Yan process, $pp \to l^+ l^- + X$, corresponds to the hard subprocess $q\bar{q} \to \gamma^* \to l^+ l^-$. The Drell Yan cross-section involves the pdf of $q$ in one of the proton, the pdf of $\bar{q}$ in the other proton and the hard subprocess cross-section, $d\hat{\sigma}$. It can be written as $d\sigma_{\text{DY}}/dQ^2 = \sum_q e_q^2 \int dx \int dy f_q(x) f_{\bar{q}}(y) d\hat{\sigma}/dQ^2$.

### 2.1.3   QCD improved parton model

QCD is a gauge theory of the strong interaction in which quarks carry a *color charge* and interact by gluon exchanges. In contrast with QED, which is based on the $U(1)$ group, QCD is based on a non abelian group, $SU(3)$. As a consequence gluons carry a color charge, there exists a three gluon vertex and the coupling constant of strong interaction, $\alpha_s$, is a decreasing function of energy. Quantities characterized by a low energy scale are called *soft*. For soft quantities, $\alpha_s$ is of order unity and perturbative calculations are not possible. It is not possible, for instance, to compute perturbatively the structure of hadrons in terms of their constituting quarks and gluons. Quantities characterized by a large energy scale are called *hard* and they can be perturbatively computed, one can compute for instance quark-quark scattering cross-sections at high enough energy. In order to reach the hard perturbative region the energy should be much larger than the characteristic energy $\Lambda_{QCD} \approx 200$ MeV. The precise limit is a matter of some debate, it should come from phenomenological studies and will depend on the considered reaction

(typically at which energy the scaling behavior predicted by QCD starts to appear). For DIS the scale is defined by $Q^2$ and a limit $Q^2 > 1$ GeV$^2$ is often used.

Free quarks or gluons have never been observed, they only appear as hadron constituents, a property which is known as *confinement*. A real process is always a process in terms of hadrons and even at high energy the computation of the cross section involves some hadron structure which cannot be computed in perturbative QCD (pQCD). For DIS and many other processes it was, however, demonstrated that the cross section can be factorized in terms of the cross section of a hard subprocess (involving quarks and gluons and computed in pQCD), and soft contributions (typically pdf's) which parametrize the hadron structure. The standard parton model then appears as equivalent to the leading order (LO) of QCD. A QCD improved version of the parton model can be defined by taking some higher order effects into account.

Beyond leading order, when one goes to next to leading order (NLO), different schemes can be introduced to perform this factorization between soft and hard contributions. In each scheme there is a factorization scale which defines the limit between the hard cross-section, calculable in pQCD, and the soft part which is included in the pdf. The pdf's depend on the factorization scheme and scale. The expression of the cross section in terms of the pdf's also depends on the factorization scheme and scale, in such a way that in the end the cross sections are independent of the scheme (which they should be since they are directly measurable quantities).

We mentioned that in the parton model the pdf's are $Q^2$ independent. However, when $Q^2$ is increased the resolution of the probe increases: what appeared for instance as a quark at a given scale, may appear like a quark together with a virtual gluon it has emitted. This results in some slow, logarithmic, variations of the pdf's with $Q^2$. In QCD, this is described by the splitting functions, $P_{qq}$, $P_{qg}$, $P_{gq}$ and $P_{gg}$ where $P_{gq}$, for instance, corresponds to the possibility for a quark to emit a gluon. The $Q^2$ evolution of the pdf's is described by the DGLAP equations [9]. To write down these equations we must consider $SU(3)$ flavor symmetry which is a symmetry between the three low mass quark flavors $u$, $d$ and $s$. One can distinguish flavor singlet (S) combinations of pdf's with all coefficients identical, like $\Sigma = u + d + s$, and non-singlet (NS) combinations with a sum of the coefficients which is zero, like $u - d$ or $u + d - 2s$. Since $P_{gq}$ is the same for $u$ and $d$ the net probability for $u - d$ to emit a gluon is zero and the $Q^2$ evolution of non-singlet distributions decouples from the gluon distribution. The DGLAP equation for the non-singlet combinations is then

$$\frac{d}{d \ln Q^2} \; q^{\mathrm{NS}}(x, Q^2) = \frac{\alpha_s(Q^2)}{2\pi} P_{qq}^{\mathrm{NS}} \otimes q^{\mathrm{NS}}, \qquad (2.6)$$

where the convolution product is defined as $[f \otimes g](x) = \int_x^1 \frac{dy}{y} f(\frac{x}{y}) g(y)$. The $Q^2$ evolutions of the gluon and the singlet distributions are described by a set of coupled equations:

$$\frac{d}{d \ln Q^2} \left( \begin{array}{c} \Sigma(x, Q^2) \\ g(x, Q^2) \end{array} \right) = \frac{\alpha_s(Q^2)}{2\pi} \left( \begin{array}{cc} P_{qq}^{\mathrm{S}} & 2n_f P_{qg} \\ P_{gq} & P_{gg} \end{array} \right) \otimes \left( \begin{array}{c} \Sigma(x, Q^2) \\ g(x, Q^2) \end{array} \right), \qquad (2.7)$$

where $n_f$ is the number of active flavors. If $q^{\mathrm{NS}}(x, Q^2)$, $\Sigma(x, Q^2)$ and $g(x, Q^2)$ are known at a given $Q^2$ scale, they can be computed at any other scale using the DGLAP equations.
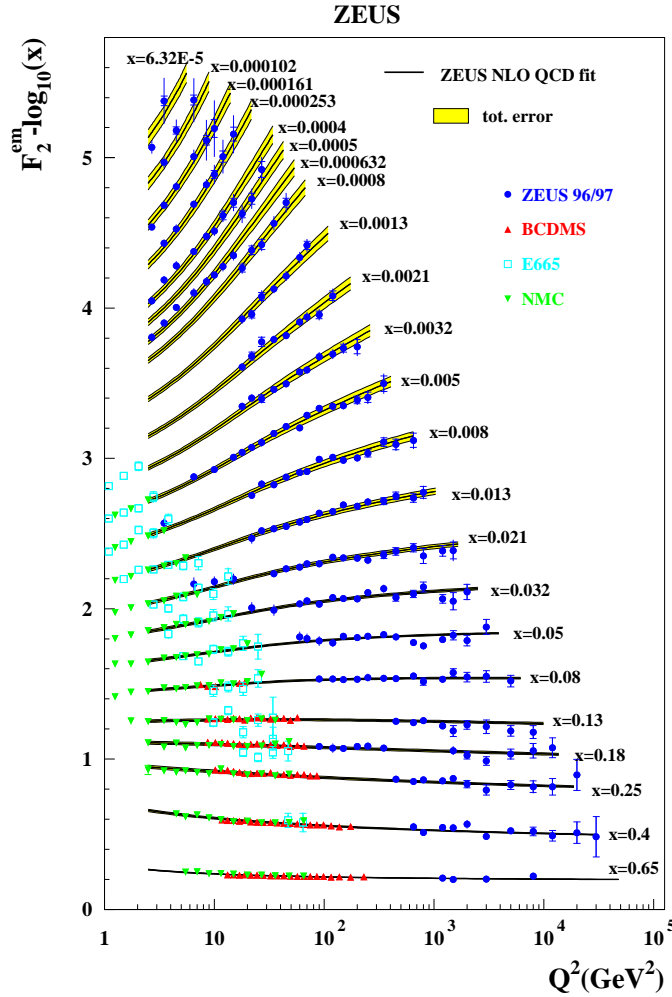
Figure 2.2: $F_2(x, Q^2)$ as a function of $Q^2$ in different $x$ bins. In order to avoid that all $x$ bins be superimposed, $F_2$ is shifted vertically by $-\log_{10}(x)$. Collider data from Hera/Zeus [10] and fixed target data from BCDMS [11], NMC [12] and E665 [13] are included, together with a QCD fit.

The structure function $F_2$ was measured both in fixed target experiments at moderate center of mass energy $\sqrt{s} = \sqrt{(k + p)^2}$ of typically 10–30 GeV and at the Hera $ep$ collider at a large $\sqrt{s}$ of 300 GeV (30 GeV positrons against 820 GeV protons). This provides measurements in a very large range of $x$ and $Q^2$. A QCD analysis of all data can be performed. One starts from a parametrization at a given scale $Q_0^2$ of $q^{\mathrm{NS}}(x, Q_0^2)$, $\Sigma(x, Q_0^2)$ and $g(x, Q_0^2)$. The pdf's are evolved to the $Q^2$ of the data using DGLAP equations, they are used to compute $F_2$ and the result is compared to the data to compute a $\chi^2$. Then the parameters are varied in order to minimize this $\chi^2$.

Fig. 2.2 shows that the DGLAP equations perfectly describe the data over the whole kinematic range. Furthermore, this means that the experimentally measured scaling violations of $F_2$ were actually able to constrain the gluon distribution through the DGLAP
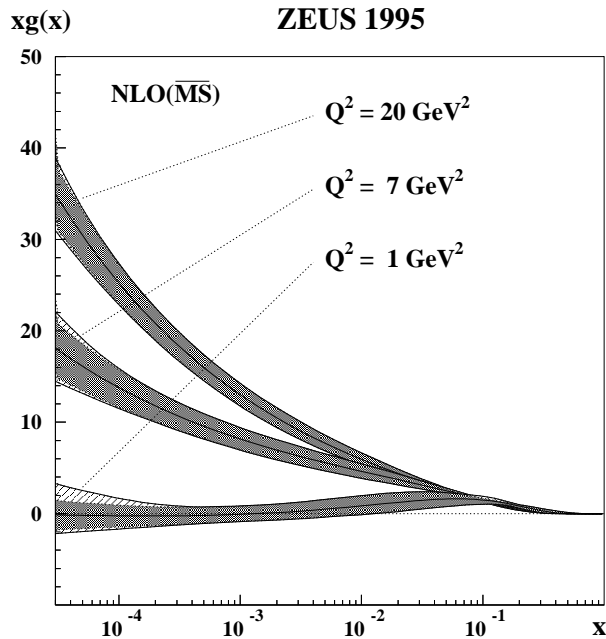
Figure 2.3: The gluon distribution at NLO in the $\overline{MS}$ scheme obtained from the scaling violations of $F_2(x, Q^2)$ using the DGLAP equations [9].

equations. This indeed provides a measurement of $g(x, Q^2)$ as illustrated in Fig 2.3.

## 2.1.4   Operator product expansion and sum rules

Rather than using the (QCD improved) parton model one can adopt a much more fundamental approach and derive sum rules for the structure functions directly from QCD using the *operator product expansion* (OPE). For a detailed and pedagogical discussion of the OPE see Ref. [14]. In the limit $x \to 0$ the product of two operators can be expanded in local operators as

$$lim_{x \to 0} \mathcal{O}_a(x)\mathcal{O}_b(0) = \sum_k c_{abk}\mathcal{O}_k(0), \tag{2.8}$$

where the Wilson coefficients $c_{abk}$ can be computed in pQCD. This can be applied to the forward Compton scattering amplitude

$$(T_{\mu\nu})_{\lambda\lambda'} = \langle p, \lambda'|t_{\mu\nu}|p, \lambda\rangle = i \int d^4x e^{iqx}\langle p, \lambda'|T(j_\mu(x), j_\nu(0))|p, \lambda\rangle \tag{2.9}$$

if $q$ is large enough, i.e. $q \gg \Lambda_{\mathrm{QCD}}$.

The local operators involved are quark and gluon operators of arbitrary dimension $d$ and spin $n$. By dimensional analysis it can be shown that these operators contribute to $l_{\mu\nu}W^{\mu\nu}$ as $(Q/M)^{2-t}$, where $t = d - n$ is the operator twist. The lowest possible value of $t$ is 2. Twist-2 operators contribute a finite amount, while higher twist contributions are reduced by powers of $Q/M$.

The twist-2 quark vector operator $\mathcal{O}_{V,n}$ of spin $n$ (and dimension $n+2$) involves $\bar{\psi}\gamma_{\mu_1}D_{\mu_2}\ldots D_{\mu_n}\psi$ and we label $V_n$ its matrix elements on the nucleon, $V_n = \langle N|\mathcal{O}_{V,n}|N\rangle$. The axial operator $\mathcal{O}_{A,n}$ involves in addition a $\gamma_5$ matrix and we label its matrix element $A_n$. Twist-2 operators correspond to the first two graphs of Fig 2.4. Twist-3 operators involve for instance $\bar{\psi}\gamma_\mu G\psi$ and correspond to graphs like the last graph of Fig 2.4.
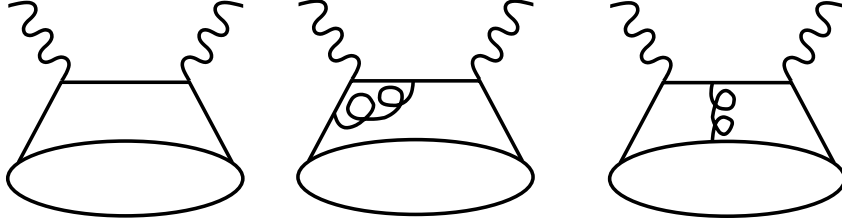


Figure 2.4: The first diagram corresponds to leading twist and leading order. The second diagram is still at leading twist but it includes higher order corrections and is reduced by a factor $\alpha_s/2\pi$. The last diagram is a higher twist contribution reduced by a factor $M/Q$.

The OPE provides an expansion of $T_{\mu\nu}$ in terms of $\omega = 1/x$. Using the optical theorem and contour integration in the complex $\omega$-plane, this can be transformed in sum rules for the structure functions:

$$2\int_0^1 x^{n-1}F_1 = C_n^{(1)}V_n \quad \text{and} \quad 2\int_0^1 x^{n-1}F_2/2x = C_n^{(2)}V_n \quad \text{(for n even)} \tag{2.10}$$

At leading order $C_n^{(1)} = C_n^{(2)}$, which gives back the Callan Gross relation, $F_2 = 2xF_1$, or $R = 0$. Going to higher order, the measurement of $F_2$ provides the $V_n$, which by inverse Mellin transform provides a prediction for $F_1$ or $R$.

## 2.1.5   QED radiative corrections

Fig. 2.5 presents the set of QED diagrams contributing to DIS cross-section up to order $\alpha^3$. They include the first order diagram (a) in $e^2$, which contributes to the cross section at the $\alpha^2$ order; the emission of real photons (d and e) in $e^3$, which contribute at the $\alpha^3$ order; and virtual corrections (b and c) in $e^4$ which enter the cross section at the $\alpha^3$ order through their interference with the first order diagram.

In addition to the radiative corrections at vertex which are called internal radiative corrections, there are external radiative corrections due to bremsstrahlung of the incident or scattered leptons on other nucleons or nuclei. These corrections are quite important with an electron beam but muon external radiations are smaller by a factor $(m_\mu/m_e)^2 = 42,000$ and are negligible. The internal corrections are proportional to $\ln(Q^2/m^2 - 1)$. At a given $Q^2$, internal corrections for muons are smaller than for electrons by typically a factor 3, but they are not negligible.
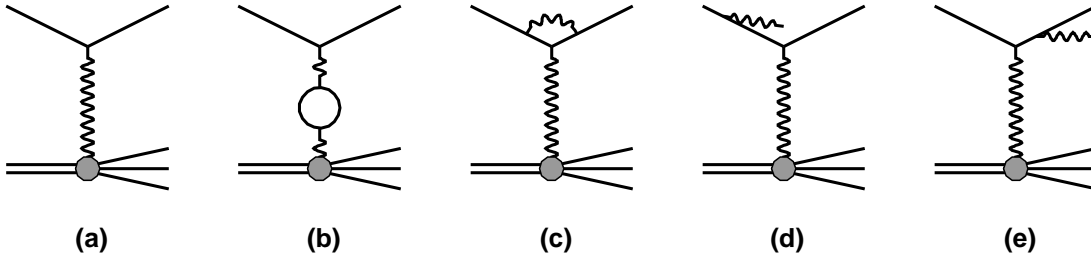
Figure 2.5: Diagrams contributing to radiative corrections at the $\alpha^3$ order.

The virtual corrections affect the cross section, while the emission of a real photon affects both the cross section and the kinematics. The apparent $x$ and $Q^2$ obtained from the measured incident and scattered leptons are smaller than the real $x$ and $Q^2$ at the virtual photon quark vertex [4]. In practice we only know the apparent kinematics. This means that experimentally the elastic peak, which should appear like a Dirac function at $x = 1$, is accompanied by a radiative tail at lower $x$ which appears like a contribution to DIS cross-section. Furthermore, by selecting a range in $\nu$ the experimental acceptance correlates $x$ and $Q^2$ (since $Q^2 = 2M\nu x$). At $x = 1$ the acceptance selects large $Q^2$ and due to the form factor the elastic cross-section is very small. At low $x$ we select small $Q^2$ and see the radiative tail from an elastic peak at small $Q^2$ where the cross section is large. So, within the experimental acceptance, the contribution of the radiative elastic tail at low $x$ is quite important whereas the elastic peak itself is negligible. The DIS cross-section itself comes with a radiative tail, but without effects due to $Q^2$, so it dies out rapidly since the probability to emit a real photon goes like the inverse of the photon energy.

## 2.2 Inclusive polarized DIS

We now turn to the polarized case, and start with the polarized structure functions. See section 2.1 and 2.1.1 for the definitions of the kinematic variables.

### 2.2.1 Structure functions

We introduce the spin four-vector $s_\mu$, such that $s^2 = -1$ and $s.k = 0$; in the particle center of mass $s = (0, 0, 0, 1)$ if the spin is along the $z$ axis. In the polarized case the leptonic tensor includes an antisymmetric term, which is proportional to the spin:

$$L_{\mu\nu} = 2 \left[ k_\mu k'_\nu + k'_\mu k_\nu - g_{\mu\nu} (kk' - m^2) + im\epsilon_{\mu\nu\alpha\beta} s^\alpha q^\beta \right], \qquad (2.11)$$

where $\epsilon_{\mu\nu\alpha\beta}$ is the Levi-Civita tensor, antisymmetric in the exchange of any component and such that $\epsilon_{1234} = 1$.

---

[4]If we label $q$ and $q'$ the virtual and the real photons, the apparent $Q^2$ is $Q_a^2 = -(q + q')^2 = Q^2 - 2qq' + 0 < Q^2$ since $qq' = q_0 q'_0 - \vec{q}\vec{q}' = q'_0(q_0 - |\vec{q}| \cos\theta_{\vec{q}\vec{q}'}) > 0$ and $x_a = \frac{Q_a^2}{2M(q_0 + q'_0)} < \frac{Q^2}{2M(\nu + q'_0)} < x$.

After imposing the same general requirements as in the unpolarized case, but keeping the antisymmetric terms, the most general form for the hadronic tensor is

$$W^{\mu\nu} = W_1 \left[ -g^{\mu\nu} + \frac{q^\mu q^\nu}{q^2} \right] + \frac{W_2}{M^2} \left( p^\mu - \frac{pq}{q^2}q^\mu \right) \left( p^\nu - \frac{pq}{q^2}q^\nu \right) + i\epsilon_{\mu\nu\alpha\beta} \frac{q^\alpha}{pq} \left[ s^\beta g_1 + \left( s^\beta - \frac{sq}{pq}p^\beta \right) g_2 \right].$$

Here also, the antisymmetric terms are proportional to the spin; they include two new structure functions, $g_1$ and $g_2$.

The lepton beam is longitudinally polarized, i.e. (anti)parallel to the beam direction. When the target is also longitudinally polarized the difference of cross sections for parallel and anti-parallel spins of the lepton and the nucleon is

$$\frac{d^2\Delta\sigma_\parallel}{dx dQ^2} = \frac{16\pi\alpha^2 y}{Q^4} \left[ \left( 1 - \frac{y}{2} - \frac{\gamma^2 y^2}{4} \right) g_1(x, Q^2) - \frac{\gamma^2 y}{2} g_2(x, Q^2) \right]. \tag{2.12}$$

With a target polarized transversely to the beam direction, the difference of cross sections depends on the angle $\phi$ between the scattering plane and the plane which includes the beam and the nucleon spin:

$$\frac{d^3\Delta\sigma_T}{dx dQ^2 d\phi} = -\cos\phi \frac{8\alpha^2 y}{Q^4}\gamma\sqrt{1 - y - \frac{\gamma^2 y^2}{4}} \left( \frac{y}{2}g_1(x, Q^2) + g_2(x, Q^2) \right). \tag{2.13}$$

In these formulas terms in $m_l^2/Q^2$ were neglected, see Ref. [15] for the full formulas.

In the parton model, where $F_1(x) = \frac{1}{2}\sum_q e_q^2[q(x) + \bar{q}(x)]$ and $F_2 = 2xF_1$, we have for the polarized structure functions:

$$g_1(x) = \frac{1}{2}\sum_q e_q^2[\Delta q(x) + \Delta\bar{q}(x)] \quad \text{and} \quad g_2(x) = 0. \tag{2.14}$$

Here, $\Delta q(x) = q^+(x) - q^-(x)$, where $q^+(x)$ and $q^-(x)$ represent the number of quarks of flavor $q$, carrying a fraction $x$ of the proton momentum, with a spin parallel $(q^+)$ and anti-parallel $(q^-)$ to the spin of the nucleon.

We now introduce the first moment, $\Gamma_1 = \int_0^1 g_1(x)dx$, and $\Delta q = \int_0^1 [\Delta q(x) + \Delta\bar{q}(x)]dx$. Note that $\Delta q$ includes both $q$ and $\bar{q}$ contributions; this is the usual notation although it can be confusing. $\Delta q$ is the difference between the number of quarks of flavor $q$ with spin parallel and with spin anti-parallel, whatever their momentum fraction $x$. This is the total contribution of the spin of flavor $q$ to the spin of the nucleon. We get

$$\Gamma_1 = \frac{1}{2}\sum_q e_q^2\Delta q = \frac{1}{2}\left[ \frac{4}{9}\Delta u + \frac{1}{9}\Delta d + \frac{1}{9}\Delta s \right]. \tag{2.15}$$

## 2.2.2   Asymmetries

The optical theorem relates the total virtual-photon absorption cross-section to the imaginary part of the forward Compton amplitudes, $\mathcal{A}_{\Lambda\lambda,\Lambda'\lambda'}$, where $\Lambda$ is the helicity of the

photon and $\lambda$ that of the nucleon. Requiring helicity conservation ($\Lambda + \lambda = \Lambda' + \lambda'$) and imposing parity ($\mathcal{A}_{\Lambda\lambda,\Lambda'\lambda'} = \mathcal{A}_{-\Lambda-\lambda,-\Lambda'-\lambda'}$) and time reversal ($\mathcal{A}_{\Lambda\lambda,\Lambda'\lambda'} = \mathcal{A}_{\Lambda'\lambda',\Lambda\lambda}$) invariances we are left with only 4 independent amplitudes. These amplitudes (and the corresponding virtual-photon absorption cross-sections) are related to the 4 structure functions by:

$$
\begin{aligned}
\sigma_{3/2}^{T} &= \frac{4\pi^2\alpha}{K}\mathcal{A}_{1\frac{1}{2}1\frac{1}{2}} &&= \frac{4\pi^2\alpha}{MK}(F_1 + g_1 - \gamma^2 g_2), \\
\sigma_{1/2}^{T} &= \frac{4\pi^2\alpha}{K}\mathcal{A}_{1-\frac{1}{2}1-\frac{1}{2}} &&= \frac{4\pi^2\alpha}{MK}(F_1 - g_1 + \gamma^2 g_2), \\
\sigma^{TL} &= \frac{4\pi^2\alpha}{K}\mathcal{A}_{1-\frac{1}{2}0\frac{1}{2}} &&= \frac{4\pi^2\alpha}{MK}\gamma(g_1 + g_2), \\
\sigma^{L} &= \frac{4\pi^2\alpha}{K}\mathcal{A}_{0\frac{1}{2}0\frac{1}{2}} &&= \frac{4\pi^2\alpha}{MK}\left[(1+\gamma^2)\frac{F_2}{2x} - F_1\right],
\end{aligned}
$$

where $K = \nu + q^2/2M$ according to Hand convention [16] [5]; $\sigma_{3/2}^T$ and $\sigma_{1/2}^T$ are the transverse virtual-photon absorption cross-sections when the sum of the spin projection are $3/2$ and $1/2$, respectively. Note that the so-called transverse photons have a spin (anti)parallel to the momentum while longitudinal photons have a spin perpendicular to the momentum. The point is that transverse and longitudinal refer to the polarization vector $\epsilon$ not to the spin [6]. The spin average, $\sigma^T = \frac{1}{2}(\sigma_{3/2}^T + \sigma_{1/2}^T) = \frac{4\pi^2\alpha}{MK}F_1$, involves only unpolarized structure functions. The same happens for the longitudinal virtual-photon absorption cross-section, $\sigma^L$, which is spin independent. Its ratio to $\sigma^T$ gives $R = (1+\gamma^2)\frac{F_2}{2xF_1} - 1$ Finally, $\sigma^{TL}$ is an interference term between the transverse and the longitudinal cross-sections.

The virtual-photon asymmetries are defined as

$$
A_1 = \frac{\sigma_{1/2}^T - \sigma_{3/2}^T}{\sigma_{1/2}^T + \sigma_{3/2}^T} = \frac{g_1 - \gamma^2 g_2}{F_1}, \qquad\qquad A_2 = \frac{\sigma^{TL}}{\sigma^T} = \gamma\frac{g_1 + g_2}{F_1}, \qquad (2.16)
$$

from which one can derive the upper limit, $|A_2| \leq \sqrt{\sigma^T\sigma^L}/\sigma^T = \sqrt{R}$, $R$ itself being small. Actually one can show [17] that $\sigma^{TL} \leq \sqrt{\sigma_{1/2}^T/2\sigma^L}$ which gives a better upper

---

[5]virtual-photon absorption cross-sections are ambiguous quantities, one can always change their definition by a factor if the definition of the flux of virtual photons $\Gamma$ is also changed in such a way that the product $\Gamma\sigma_\gamma$, which is the measurable lepton-nucleon cross-section, is unchanged. This ambiguity is embedded in the factor $K$. The ambiguity vanishes in the limit of real photons ($Q^2 = 0$) since $\Gamma$ and $\sigma_\gamma$ are then both independently measurable. In this case we must have $K = \nu = |q|$ and then $W^2 = M^2 + 2MK$. Hand convention consists in keeping this last relation valid for all $Q^2$, i.e. $K = (W^2 - M^2)/2M = \nu + q^2/2M$

[6]The photon field is $A^\mu = \epsilon^\mu e^{iqx}$. The Lorentz gauge condition $\partial_\mu a^\mu = 0$ then gives $q_\mu\epsilon^\mu = 0$. Real photons have $m_\gamma = 0$ which gives a second constraint on $\epsilon$, namely $\vec{q}.\vec{\epsilon} = 0$. There remain only 2 degrees of freedom for the polarization vector, $\epsilon_1$ and $\epsilon_2$, such that $\vec{\epsilon_1}.\vec{q} = 0$ and $\vec{\epsilon_2}.\vec{q} = 0$. Since the polarization vector is perpendicular to the momentum real photons are said to be *transverse*.
There is no constraint on the mass for virtual photons and a third direction of polarization appears $\vec{\epsilon_3} \parallel \vec{q}$.
A virtual photon can be transverse ($\epsilon_1$ or $\epsilon_2$) or *longitudinal* ($\epsilon_3$).
We can define circular polarizations $\epsilon_L = (\epsilon_1 - \imath\epsilon_2)/\sqrt{2}$ and $\epsilon_R = (\epsilon_1 + \imath\epsilon_2)/\sqrt{2}$. Helicity is the projection of the spin on the momentum. $\epsilon_R$ has helicity $+1$, $\epsilon_L$ $-1$ and $\epsilon_3$ zero.
So transverse photons have a spin (anti)parallel to the momentum while longitudinal photons have a spin perpendicular to the momentum ! The point is that transverse and longitudinal refer to the polarization vector $\epsilon$, but not to the spin.

limit, $|A_2| \leq \sqrt{R(1 + A_1)/2}$. In practice it is found that $A_2$ is even much smaller than this upper limit.

Experimentally one measures lepton-nucleon asymmetries, defined as $A_{\parallel} = \Delta\sigma_{\parallel}/2\sigma$ and $A_{\perp} = \Delta\sigma_{\perp}/(2\sigma\cos\phi)$. They are related to the virtual-photon asymmetries through $A_{\parallel} = D(A_1 + \eta A_2)$ and $A_{\perp} = d(A_2 - \xi A_1)$ where $\eta \ll 1$ and $\xi \ll 1$ are kinematic factors. So in practice $A_{\parallel} \approx DA_1$ and $A_{\perp} \approx dA_2$. The factor $D \approx \frac{1-(1-y)^2}{1+(1-y)^2} \approx y$ is the *virtual photon depolarization factor*, which accounts for the fact that only a part of the lepton polarization is translated to the virtual photon. See Ref. [15] for the expressions of $d$, $\eta$ and $\xi$ and the full expression of $D$, including $m_l^2/Q^2$ terms.

### 2.2.3   Intuitive approach

We will use the *Breit frame* where the quark momenta before and after the virtual photon absorption are such that $p' = -p$ (this frame is also called the *brick wall frame*). Let us first consider the absorption of a transverse virtual photon with spin projection $m_{\gamma} = +1$ by a quark. If the spin projection of the quark is $m_q = -1/2$ (Fig. 2.6 left), the total projection is $1/2$ and the absorption can occur. If the spin projection of the quark is $m_q = +1/2$ (Fig. 2.6 right), the total projection is $3/2$, the final quark cannot have $m_q = 3/2$ and the absorption cannot occur. The $m_{\gamma} = +1$ photon "sees" only $m_q = -1/2$ quarks.
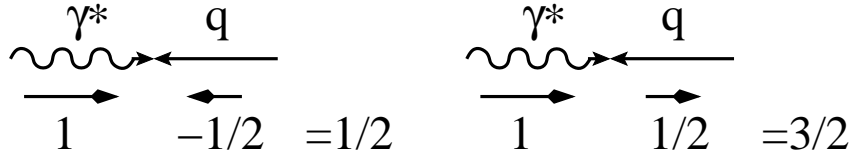


Figure 2.6: Spin projections in the Breit frame. The absorption of the photon by the quark is only possible in the case on the left.

If we consider a set of quarks embedded inside a $m_N = -1/2$ nucleon (Fig. 2.7 left), the $m_{\gamma} = +1$ photon will filter out $m_q = -1/2$ quarks, i.e. quark with spin parallel to the spin of the nucleon. So the corresponding photon-nucleon cross-section, which we label $\sigma_{1/2}$ since the total spin projection of the photon and the nucleon is $1/2$, is proportional to the pdf of quarks with spin parallel to the spin of the nucleon, $\sigma_{1/2} \propto q^+(x)$. Conversely, $\sigma_{3/2} \propto q^-(x)$, as can be seen on Fig. 2.7 right. So $F_1 \propto (\sigma_{1/2} + \sigma_{3/2})$ counts quarks independently of their spin, $F_1(x) = \frac{1}{2}\left[\frac{4}{9}(u(x) + \bar{u}(x)) + \frac{1}{9}(d(x) + \bar{d}(x)) + \frac{1}{9}(s(x) + \bar{s}(x))\right]$, whereas $g_1 \propto (\sigma_{1/2} - \sigma_{3/2})$ measures the difference between the number of quarks with spin parallel and with spin anti-parallel

$$g_1 = \frac{1}{2}\left[\frac{4}{9}(\Delta u(x) + \Delta\bar{u}(x)) + \frac{1}{9}(\Delta d(x) + \Delta\bar{d}(x)) + \frac{1}{9}(\Delta s(x) + \Delta\bar{s}(x))\right]. \qquad (2.17)$$
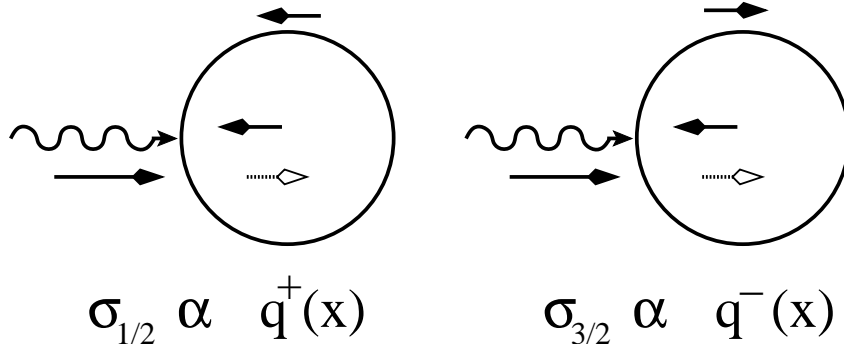
$$\sigma_{1/2} \ \alpha \ q^+(x) \qquad \sigma_{3/2} \ \alpha \ q^-(x)$$

Figure 2.7: Absorption of a polarized photon by a polarized nucleon.

### 2.2.4 QCD improved parton model

In QCD the relationship between $g_1$ and the pdf's is more involved:

$$g_1(x, Q^2) = \frac{1}{2} \langle e^2 \rangle \left[ C_q^S \otimes \Delta\Sigma + 2n_f C_g \otimes \Delta g + C_q^{NS} \otimes \Delta q_{NS} \right], \qquad (2.18)$$

where $\langle e^2 \rangle = \frac{\sum_{k=1}^{n_f} e_k^2}{n_f}$, $\Delta q_{NS} = \sum (\frac{e_k^2}{\langle e^2 \rangle} - 1)\Delta q_k$, and the C's are the so-called Wilson coefficients, computable in pQCD. At LO $C_q^S = C_q^{NS} = \delta(1 - x)$ and $C_g = 0$ so that one finds back the naive parton model result, (Eq. 2.17).

As in the unpolarized case the $Q^2$ evolution of the NS distribution is decoupled from the gluon:

$$\frac{d}{d \ln Q^2} \ \Delta q^{NS}(x, Q^2) = \frac{\alpha_s(Q^2)}{2\pi} P_{qq}^{NS} \otimes \Delta q^{NS}, \qquad (2.19)$$

while the $Q^2$ evolutions of the gluon and the singlet distributions are described by a set of coupled equations:

$$\frac{d}{d \ln Q^2} \begin{pmatrix} \Delta\Sigma(x, Q^2) \\ \Delta g(x, Q^2) \end{pmatrix} = \frac{\alpha_s(Q^2)}{2\pi} \begin{pmatrix} P_{qq}^S & 2n_f P_{qg} \\ P_{gq} & P_{gg} \end{pmatrix} \otimes \begin{pmatrix} \Delta\Sigma(x, Q^2) \\ \Delta g(x, Q^2) \end{pmatrix}. \qquad (2.20)$$

All Wilson coefficients [18] and splitting functions [19] have been computed to NLO.

### 2.2.5 Sum rules

The operator product expansion (OPE, see section 2.1.4) provides sum rules which relate a moment of a structure function to the *matrix element* of an operator on the nucleon, $\langle N|\mathcal{O}|N \rangle$. For the first moment of $g_1$ we get at leading order

$$\Gamma_1^p = \int_0^1 g_1(x) dx = \frac{1}{2} \left[ \frac{4}{9} a_u + \frac{1}{9} a_d + \frac{1}{9} a_s \right] \quad \text{(leading order)},$$

where $a_q s^\mu = \langle N|\bar{q}\gamma_\mu\gamma_5 q|N \rangle$ is the *axial matrix element* of the nucleon for flavor $q$. Multiplicative corrections appear at higher order in the form of Wilson coefficients $C_1$, which

are different for singlet and non-singlet terms. In a "naive" interpretation $a_q = \Delta q$, the total contribution of the spin of flavor $q$ to the spin of the nucleon, and we find back the result of the parton model (Eq. 2.15).

The $a_q$ can be combined according to $SU(3)$ flavor symmetry. There is a *singlet* combination $a_0 = a_u + a_d + a_s$ and *non-singlet* combinations $a_3 = a_u - a_d$ (triplet) and $a_8 = a_u + a_d - 2a_s$ (octet). At this stage this is just a labeling, which does not imply that the $SU(3)$ flavor symmetry is exact.

The isospin symmetry (or flavor $SU(2)$) between the $u$ and $d$ flavors is valid to a very good approximation. Proton and neutron are symmetric states in terms of isospin, meaning for instance $a_u^p = a_d^n$ and $a_s^p = a_s^n$. We take the proton as reference: $a_i := a_i^p$, e.g. $a_u := a_u^p = a_d^n$. The OPE result can then be written as:

$$\Gamma_1^{p(n)} = C_1^{\mathrm{NS}} \left[ +(-)\frac{1}{12}a_3 + \frac{1}{36}a_8 \right] + \frac{1}{9}C_1^{\mathrm{S}}a_0, \qquad (2.21)$$

with the singlet $C_1^{\mathrm{S}}$ and non-singlet $C_1^{\mathrm{NS}}$ Wilson coefficients. At NLO they are equal, $C_1 = 1 - \alpha_s(Q^2)/\pi$, but they differ at higher orders [18]. Using isospin rotation of electromagnetic and weak current (current algebra) Bjorken showed that $a_u - a_d = \langle p|\bar{u}\gamma^\mu\gamma_5 u - \bar{d}\gamma^\mu\gamma_5 d|p\rangle$ equals the neutron weak decay constant $g_A/g_V = \langle p|\bar{u}\gamma^\mu\gamma_5 d|n\rangle$ [1]. Since the neutron decay constant is measured, $g_A/g_V = 1.2573 \pm 0.0028$, this provides a prediction which is known as the Bjorken sum rule [20] and is a fundamental prediction of QCD, requiring only isospin invariance:

$$\Gamma_1^p - \Gamma_1^n = \frac{1}{6}(a_u - a_d)C_{NS} = \frac{1}{6}\frac{g_A}{g_V}C_{\mathrm{NS}}. \qquad (2.22)$$

Flavor $SU(3)$ symmetry is more approximate than $SU(2)$. It allows for the octet term to be linked with hyperon octet weak decay constants (octet including the nucleon, the $\Sigma$, the $\Xi$ and the $\Lambda$): $a_8 = 3F - D = 0.585 \pm 0.025$. Assuming in addition $a_s = 0$ (few $s$ quarks in the nucleon and they should not be polarized), allows for a prediction for $\Gamma_1^p$ and $\Gamma_1^n$ which is called the *Ellis-Jaffe sum rule* [21]:

$$\Gamma_1^{p(n)} = C_1^{\mathrm{NS}} \left[ +(-)\frac{1}{12}g_A/g_V + \frac{1}{36}(3F - D) \right] + \frac{1}{9}C_1^{\mathrm{S}}(3F - D). \qquad (2.23)$$

This assumption $a_s = 0$ also provides, together with $a_3 = g_A/g_V$ and $a_8 = 3F - D$, 3 equations for the 3 unknowns, $a_u$, $a_d$ and $a_s$. In particular it gives $a_0 = a_8 = 3F - D$. So, before the EMC result the expectation was $\Delta\Sigma = a_0 \approx 0.6$, in qualitative agreement with the QM.

## 2.2.6   The spin crisis

The EMC experiment [2] measured $\Gamma_1^p$ and found a violation of the Ellis-Jaffe sum rule. This came as a big surprise. It implied that the hypothesis $a_s = 0$ had to be released. Instead the measurement of $\Gamma_1^p$ had to be used as the third equation, together with $a_3 =$

$g_A/g_V$ and $a_8 = 3F - D$, for the extraction of the 3 unknowns, $a_u$, $a_d$ and $a_s$. In the "naive" interpretation where $a_q = \Delta q$, this gave the surprising results $\Delta\Sigma = a_0 = 0.12 \pm 0.09 \pm 0.14$ and $\Delta s = a_s = -0.19 \pm 0.03 \pm 0.04$. This was confirmed later by the SMC at Cern [22, 23], by several experiments at SLAC [24] and by Hermes at Desy [25].

### 2.2.7  Axial anomaly

Classically, due to the chiral symmetry the axial current $j_5^\mu = \bar{\psi}\gamma^\mu\gamma_5\psi$ should be conserved and in this case the corresponding axial charges $a_q$ and $a_0$ should not depend on $Q^2$. At the quantum level, however, there is an anomalous, gluonic, contribution to $\partial_\mu j_5^\mu$ and the axial current is no longer conserved [26]. Due to this axial anomaly [27], $\partial a_0/\partial Q^2 \neq 0$. The gluonic contribution to $a_0$ is $-n_f \frac{\alpha_s}{2\pi}\Delta g$, where $n_f = 3$ is the number of active flavors. In addition, $\Delta g$ behaves like $1/\alpha_s$ when $Q^2 \to \infty$, so that the anomalous gluonic contribution, in spite of the $\alpha_s$ factor, is not a correction which vanishes at high $Q^2$. This makes the interpretation of $a_0$ and $a_s$ delicate. On the other hand, as already mentioned, non-singlet combinations do not couple to gluons. They are thus not affected by the axial anomaly and for instance the interpretation of $a_3$ as $\Delta u - \Delta d$ pauses no problem.
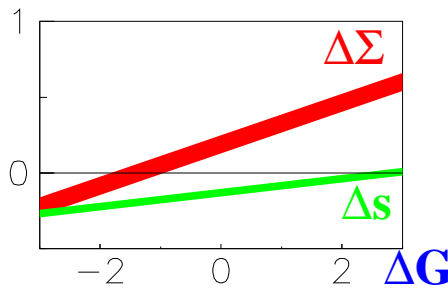


Figure 2.8: Experimentally possible values of $\Delta\Sigma$ and $\Delta s$ as a function of the assumed value of $\Delta g$.

$\Gamma_1$ or $a_q$ can be directly measured and are therefore independent of renormalization or factorization scheme or scale, whereas $\Delta\Sigma$, like any pdf, is scheme dependent. The so-called Adler-Bardeen (AB) scheme [28] is defined in order to cancel the gluonic contribution to $\Delta\Sigma$. In this scheme $\Delta\Sigma = a_0 + n_f \frac{\alpha_s}{2\pi}\Delta g$ and $\Delta s = a_s + \frac{\alpha_s}{2\pi}\Delta g$ so that $\Delta\Sigma$ and $\Delta s$ become $Q^2$ independent [7]. The AB scheme is then adequate for comparison of $\Delta\Sigma$ with the corresponding quantity in the QM which is a low scale quantity, while in other schemes $\Delta\Sigma$ undergo strong scale dependence at low $Q^2$. In these conditions the interpretation of the experimental results is illustrated in figure 2.8. If $\Delta g = 0$ the spin crisis remains, $\Delta\Sigma \approx 0.2$ and $\Delta s \approx -0.1$. If $\Delta g$ is large enough and positive, in spite of the measured values of $a_s$ and $a_0$, we may have $\Delta s \approx 0$ and $\Delta\Sigma \approx 0.6$, in qualitative agreement with the corresponding constituent quark contribution in the QM.

A measurement of $\Delta g$ then appears to be needed, both for itself, as an element of the nucleon spin puzzle, and in order to be able to extract $\Delta\Sigma$ and $\Delta s$ from the $g_1$ data.

---

[7]This is not the case of the $\overline{MS}$ scheme [29] in which $\Delta\Sigma = a_0$ and $\Delta s = a_s$, and then $\partial\Delta\Sigma/\partial Q^2 \neq 0$

## 2.3   Semi-Inclusive polarized DIS

We now discuss what can be learned by requiring a hadron in coincidence with the scattered lepton, $l + p \to l + h + X$. We introduce the Feynman variable, $x_F = 2p_\parallel^*/W$, where $p_\parallel^*$ is the hadron momentum projected along the virtual photon momentum, estimated in the photon-nucleon center of mass frame. $x_F$ is actually the ratio of $p_\parallel^*$ to the maximum value it can reach (i.e. $W/2$), so $-1 \le x_F \le 1$. In this frame the quark which absorbed the virtual photon has $p_\parallel^* > 0$, whereas the other quarks continue in the initial nucleon direction and have $p_\parallel^* < 0$ (see Fig. 2.9). Hadrons with $p_\parallel^* > 0$ (and then $x_F > 0$) come from the hadronization of the quark which absorbed the photon (kinematic region of *current fragmentation*) whereas hadrons with $p_\parallel^* < 0$ come from the *target fragmentation* region ($x_F < 0$). Of course this is an oversimplified picture and there is not a clear cut at $x_F = 0$, but requiring e.g. $x_F > 0.2$ selects a sample hopefully dominated by current fragmentation region.



Figure 2.9: photoabsorption in the photon nucleon rest frame. Before the photoabsorption (left) all quarks have a negative $p_\parallel^*$. Then the quark which absorbed the photon has a positive $p_\parallel^*$ while the remaining spectator quarks keep a negative $p_\parallel^*$ (right).

We define the ratio $z = E_h/\nu$ of the hadron energy to the virtual photon energy and we introduce the fragmentation functions $D_q^h(z, Q^2)$ which represent the probability for a quark $q$ to produce in its fragmentation a hadron $h$ with energy $z\nu$.

Symmetries reduce the number of independent fragmentation functions. Due to $SU(2)$ symmetry $D_u^{\pi^+} = D_d^{\pi^-}$, due to charge conjugation $D_{\bar{d}}^{\pi^-} = D_d^{\pi^+}$ and finally due to $SU(2)$ symmetry again $D_{\bar{d}}^{\pi^+} = D_{\bar{u}}^{\pi^-}$. This fragmentation function, $D_u^{\pi^+} = D_d^{\pi^-} = D_{\bar{d}}^{\pi^+} = D_{\bar{u}}^{\pi^-}$, is said to be *favored* since it corresponds to the production of a $\pi^+ = u\bar{d}$ from a $u$ quark. Similarly, we have $D_u^{\pi^-} = D_d^{\pi^+} = D_{\bar{d}}^{\pi^-} = D_{\bar{u}}^{\pi^+}$ which is the *disfavored* fragmentation function ($\bar{u}d$ from a $u$ quark). Finally, we have the *strange* fragmentation function, $D_s^{\pi^+} = D_s^{\pi^-} = D_{\bar{s}}^{\pi^+} = D_{\bar{s}}^{\pi^-}$. So we have only 3 fragmentation functions is we limit ourselves to the fragmentation to $\pi$: favored, disfavored and strange.

In the parton model

$$A_1 = \frac{F_1}{g_1} = \frac{\sum_q e_q^2 [\Delta q(x) + \Delta \bar{q}(x)]}{\sum_q e_q^2 [q(x) + \bar{q}(x)]} \tag{2.24}$$

and for the $\gamma^* + p \to h + X$ asymmetry in the $x_F > 0$ region

$$A_1^h = \frac{\sum_q e_q^2 [\Delta q(x) D_q^h(z) + \Delta \bar{q}(x) D_{\bar{q}}^h(z)]}{\sum_q e_q^2 [q(x) D_q^h(z) + \bar{q}(x) D_{\bar{q}}^h(z)]}. \tag{2.25}$$

Due to $D_u^{\pi^+} > D_{\bar{u}}^{\pi^+}$, the $A_1^h$ asymmetry distinguishes $q$ and $\bar{q}$ and allows for a separation of sea and valence. The measurement of $A_1(x)$, $A_1^{\pi^+}(x)$ et $A_1^{\pi^-}(x)$ for the proton and the

neutron provides six equations and allows for a separation of the different flavors in each $x$ bin, as detailed in section 3.3. and illustrated in Fig. 3.11.

## 2.4 The third parton distribution: transversity

As illustrated in Fig 2.10, due to the optical theorem, quark pdf's are proportional to the imaginary part of quark-nucleon forward amplitudes $\mathcal{A}_{\Lambda\lambda',\Lambda'\lambda}$. The amplitudes are labeled by the helicity of the entering nucleon ($\Lambda$) and quark ($\lambda'$) followed by that of the exiting nucleon ($\Lambda'$) and quark ($\lambda$). Note that $\lambda'$ is entering and $\lambda$ exiting. Helicity conservation then requires $\Lambda + \lambda' = \Lambda' + \lambda$. Imposing also parity and time reversal invariances we are left with only 3 independent amplitudes (see Fig. 2.11). The first two are well known, $\mathcal{A}_{++,++}$ corresponds to the $q^+(x)$ quark distribution function, $\mathcal{A}_{+-,+-}$ to $q^-(x)$. So $q(x) \propto \mathcal{I}m\,(\mathcal{A}_{++,++} + \mathcal{A}_{+-,+-})$ and $\Delta q(x) \propto \mathcal{I}m\,(\mathcal{A}_{++,++} - \mathcal{A}_{+-,+-})$. The third amplitude, $\mathcal{A}_{+-,-+}$, corresponds to a new quark distribution function called transversity and denoted $\Delta_T q$ [8]. Transversity was discovered in 1979 [30], forgotten and rediscovered in 1990 [31]. From a theoretical point of view it is as interesting as the two other pdf's, $q$ and $\Delta q$. In spite of the fact that it was not yet measured, it is now the topic of many theoretical studies and a detailed review is provided by Ref. [32].

In the helicity basis in which we have worked, $\mathcal{A}_{+-,-+}$ is an interference term and has no probabilistic interpretation. If we now turn to a transversity basis (i.e. we measure the spins along the $y$ axis, perpendicular to the momentum), defined by $|\uparrow\rangle = (|+\rangle + i|-\rangle)/\sqrt{2}$ and $|\downarrow\rangle = (|+\rangle - i|-\rangle)/\sqrt{2}$, then $q(x) \propto \mathcal{I}m\,(\mathcal{A}_{\uparrow\uparrow,\uparrow\uparrow} + \mathcal{A}_{\uparrow\downarrow,\uparrow\downarrow})$, $\Delta_T q(x) \propto \mathcal{I}m\,(\mathcal{A}_{\uparrow\uparrow,\uparrow\uparrow} - \mathcal{A}_{\uparrow\downarrow,\uparrow\downarrow})$ and $\Delta q(x) \propto \mathcal{I}m\,(\mathcal{A}_{\uparrow\downarrow,\downarrow\uparrow})$. In a transversity basis $\Delta q(x)$ becomes an interference, while $\Delta_T q(x)$ can be interpreted as the polarized quark distribution in a nucleon polarized perpendicular to its (infinite) momentum, $\Delta_T q(x) = q^\uparrow(x) - q^\downarrow(x)$.

In a non relativistic model $\Delta_T q(x) = \Delta q(x)$. However, since rotations do not commute with Lorentz boost, this is no longer the case when relativistic effects are included. An interesting feature of transversity is that gluons do not contribute to it. Due to their spin 1, the $\mathcal{A}_{+-,-+}$ amplitude for gluons does not conserve helicity: $\Lambda + \lambda' = 1/2 - 1 \neq \Lambda' + \lambda = -1/2 + 1$. In this sense transversity spin distributions are more adequate for comparisons with QM expectations than traditional quark helicity distributions, which are affected by gluonic contributions due to the axial anomaly.

### 2.4.1 How to measure transversity ?

Transversity requires the helicity of the quark to be flipped (see Fig 2.11), whereas all hard processes conserve helicity along the quark line. It is then hard to measure; it decouples for instance from inclusive DIS (Fig. 2.12 left). The helicity flip requires another soft object, besides the nucleon pdf. Semi-inclusive DIS provides such an object (Fig. 2.12 middle), the

---

[8]The notation $\delta q(x)$ is also used and the quantity $h_1(x) = \sum_q e_q^2 \Delta_T q(x)$, which is the analog of the $g_1$ structure function, is sometimes introduced.

Figure 2.10: Quark distribution functions are proportional to the imaginary part of quark-nucleon forward amplitudes $\mathcal{A}_{\Lambda\lambda',\Lambda'\lambda}$, where $\Lambda$ refers to the nucleon helicity and $\lambda$ to the quark helicity.
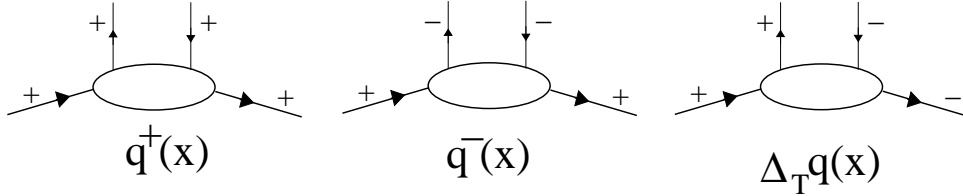


Figure 2.11: The three quark-nucleon helicity amplitudes corresponding to the $q^+$, $q^-$ and $\Delta_T q$ pdf's. For $\Delta_T q$ the helicity of the quark has to be flipped. Note the misprint in the helicity labels of $\Delta_T q$ in the corresponding figures of the review paper [32] (Figs. 1 and 9).

fragmentation function $D_q^h(z)$, which represents the probability that a quark $q$ fragments in a hadron $h$ with a fraction $z$ of the virtual photon energy. In order to measure $\Delta_T q$ we then have to find a way to measure the final quark transverse polarization. This can be done trough the measurement of the final hadron transverse polarization[9], through single pion azimuthal distribution (the so-called Collins effect [33], see section 4.4) or through two pion distributions (due to some interferences in the fragmentation process). Note that in all cases one will measure the product of $\Delta_T q(x)$ by some still unknown polarized fragmentation function. These polarized fragmentation functions can be measured in $e^+e^-$ collisions. Due to the correlation of the transverse spins of the produced $q\bar{q}$ pair, we have access to the squared of the polarized fragmentation functions.

Another possibility is that the second soft object be provided by a second nucleon pdf. The Drell-Yan process, $NN \to ll' + X$, corresponds to the hard process $q\bar{q} \to \gamma^* \to ll'$. As illustrated by the right graph of Fig. 2.12, this hard process can couple to transversity in both nucleons. In this case one measures a convolution of $\Delta_T q$ in one of the nucleons with $\Delta_T \bar{q}$ in the other nucleon and there is no unknown fragmentation function.

---

[9]this can be done for $\Lambda$ which are self analyzing particles, the measurement of the angular distribution of their decay particle provide their polarization.
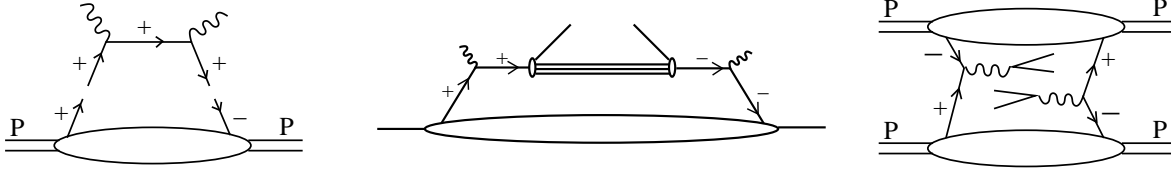
Figure 2.12: Left: In the case of inclusive DIS, the hard process (upper part) which conserves helicity cannot couple to transversity (lower part). Middle: In the case of semi inclusive DIS, the fragmentation function can flip the helicity in the upper part, allowing it to couple to transversity. Left: In the Drell-Yan process the possibility to flip the helicity is provided by the second proton pdf.

## 2.5 How to measure $\Delta g$

We concluded section 2.2 with the need to measure $\Delta g$. We will discuss the indirect measurement through the QCD analysis of $g_1$ scaling violations and direct measurements, both with the electromagnetic probe and with a *p-p* collider.

### 2.5.1 QCD analysis of $g_1$

As described in section 2.1.3 a global NLO QCD analysis of all $F_2$ data provides a good determination of $g(x, Q^2)$. Similarly we could, in principle, use the DGLAP equations to extract $\Delta g$ from $\partial g_1 / \partial \ln Q^2$. Unfortunately, in contrast with the unpolarized case for $F_2$, we do not have $g_1$ data from collider experiments and the limited range of $Q^2$ provided by the fixed target experiments does not allow for an accurate determination of $\Delta g$. This is illustrated in Fig. 3.10 from SMC QCD analysis [23] where we see that $\Delta g(x, Q^2)$ is indeed poorly determined and a direct measurement is highly desirable.

### 2.5.2 Direct measurement with electromagnetic probe

Since gluons have no electric charge they do not interact with photons at the zero[th] order. An interaction is possible at the next order through the so called *photon-gluon fusion* (PGF) process, where the photon and the gluon exchange a quark and give a $q\bar{q}$ pair in the final state, as illustrated in Fig. 2.13. In order to determine the fraction, $x_g$, of the nucleon momentum carried by the gluon we start from $\hat{s}$, the Mandelstam variable for the hard subprocess, and write $\hat{s} = (\gamma + g)^2 = (q + x_g P)^2$. We then have $\hat{s} = -Q^2 + 2x_g Pq + 0$, so

$$x_g = \frac{\hat{s} + Q^2}{2Pq}. \tag{2.26}$$

To get $x_g$ one needs to know $\hat{s} = (\gamma + g)^2 = (q + \bar{q})^2$. Since we do not directly measure the $q\bar{q}$ pair, $\hat{s}$ and then $x_g$ are not measured, but can only be estimated. Note also that, from its definition, it is clear that $x_g > x_{bj} = Q^2 / 2Pq$.
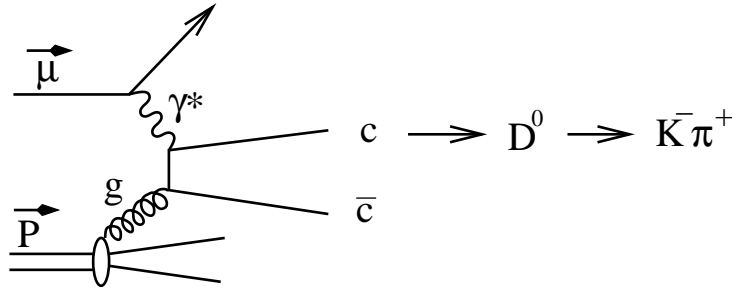
Figure 2.13: The photon gluon fusion process with production of open charm.

The probability of the PGF process is reduced by a factor $\alpha_s$ relative to the leading order (LO) photo-absorption by a quark $\gamma^* q \to q$ (Fig. 2.14 left), so we need to tag the PGF process. There are essentially two ways to do it. One possibility is to search for $c\bar{c}$ pairs. The $c$ is too heavy to contribute significantly to the nucleon wave function, it then cannot result from the LO photo-absorption process and it cannot be produced either in the ensuing fragmentation of quarks to hadrons. The $c\bar{c}$ pair can be identified through the $J/\Psi$ meson which is a $c\bar{c}$ state and can be detected very easily through its $\mu^+ \mu^-$ decay. However, the $c\bar{c}$ pair which results from the PGF process is in a color octet state and it needs to exchange another gluon to produce a $J/\Psi$ and this reaction mechanism is not well understood. On the other hand the $c$ results in 60% of the cases in a $D^0$ meson which can be identify in its two body decay channel $D^0 \to K\pi$ (4% branching ratio). The $D^0$ meson ($c\bar{u}$), in contrast with the $J/\Psi$, has a net charm, and this is called *open charm*.

For a fixed target experiment, another possibility to sign PGF is to detect a pair of hadrons with large transverse momentum $p_t$ with respect to the virtual photon direction [34] (of course at collider energies one will instead request a pair of jets at high $p_t$). In the $\gamma^* g$ center of mass frame the $q\bar{q}$ can be produced at any angle with respect to the $\gamma^*$ direction. If this angle is not close to 0 or $180^o$, the $q$ and $\bar{q}$ may indeed have a large $p_t$ which will remain in the boost to the laboratory frame. On the contrary, the quark after LO photo-absorption (Fig. 2.14 left), and the resulting hadrons, have essentially the direction of the virtual photon and small $p_t$. There is, however, a process, at the same order as PGF, which also produces high $p_t$ hadron pairs, namely QCD Compton. This is illustrated in Fig. 2.14 right: the virtual photon is absorbed by a quark which then emits a gluon. The final quark and gluon can both produce a high $p_t$ hadron. This process can fortunately be computed (since it involves the already measured polarized quark distributions) and subtracted from the measured asymmetry.

### 2.5.3   Direct measurement with $p$-$p$ collider

In $p$-$p$ collisions the quarks from one of the protons can be used to probe the gluons in the other proton through the prompt photon production process, $q + g \to q + \gamma$ (Fig. 2.15 left). So one must select $pp \to \gamma + jet + X$ events. The momentum of the quark which is probing the gluon is not known, so the measured asymmetry will be a convolution of
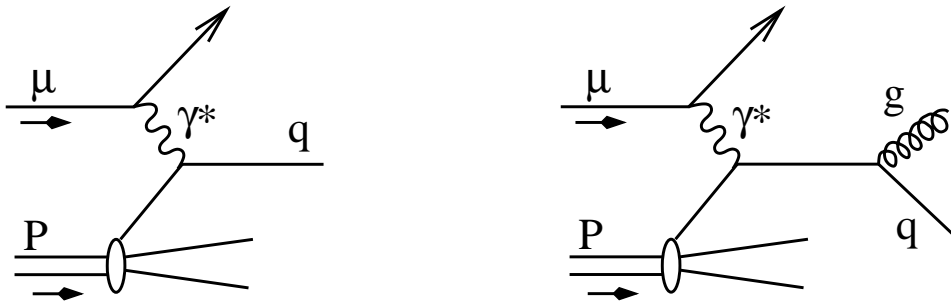
Figure 2.14: Background processes to PGF for the production of a high $p_t$ hadron pair: LO (left) and QCD Compton (right).

$\Delta q$ in one proton and $\Delta g$ in the other proton. In addition, there is a background process: $q\bar{q} \to \gamma g$ (Fig. 2.15 right). It can be computed and subtracted since it comes from the convolution of $\Delta q$ in one proton with $\Delta \bar{q}$ in the other proton.
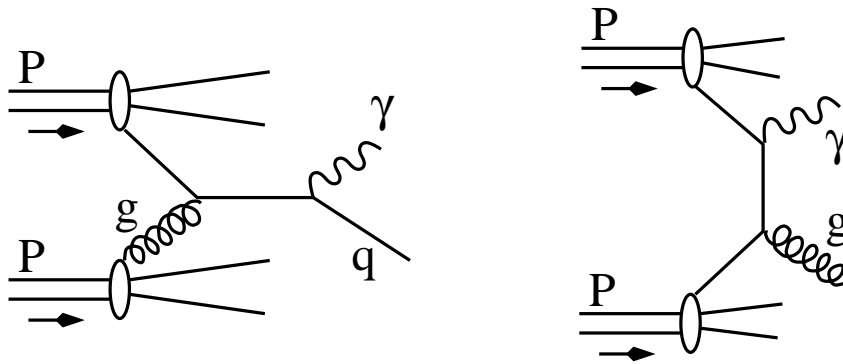


Figure 2.15: The prompt photon production (left) which allows for the measurement of $\Delta g$ in $\vec{p}\vec{p}$ collision and the background process (right).

# Chapter 3

# The SMC experiment

The EMC experiment [2] concluded that the contribution of the spin of the quark to the spin of the nucleon was small (see section 2.2). This came as a big surprise and the SMC experiment was designed to cross check this result and to make in addition a measurement of the neutron spin structure function, $g_1^n$, in order to test the fundamental Bjorken sum rule. Ref. [7] gives a detailed description of the experiment, while the final results can be found in Ref. [22] and a QCD analysis is presented in Ref. [23].

## 3.1  Experimental set-up

The SMC experiment was installed at CERN in the same hall as the EMC experiment. A large part of the EMC set-up was used. The main improvements were a new polarized target, which allowed for frequent spin reversal by reversal of the target magnetic field, and a beam polarimeter, while EMC was relying on a MC simulation of the beam-line to calculate the beam polarization.

The high energy muon beam-line, M2, starts with the 450 GeV protons from the SPS impinging on a beryllium target. About 5% of the resulting secondary pions and kaons decay into muons and neutrinos over a 600 m long channel and the remaining ones are stopped in a 9.9 m long Beryllium absorber. A beam energy of 190 GeV was selected for SMC and the intensity was $4 \times 10^7$ muons per SPS pulse (one pulse of 2.4 s every 14.4 s).

A Beam Momentum Station, located in the tunnel before the hall, measured the momentum of the incident muon for each trigger with a resolution better than 0.5%. The rest of the set-up is described below; it consists of a polarized target, a spectrometer and a beam polarimeter.

### 3.1.1   The SMC polarized target [35]

Butanol and ammonia were used as a proton target; deuterated butanol was used as a deuterium target. Some paramagnetic centers are introduced in the material either in the form of a small amount of EHBA-Cr (V) complexes for butanol or through irradiation in an electron beam for ammonia.

The target material is polarized by dynamic nuclear polarization (DNP) [36]. In a magnetic field $B$, due to the Zeeman effect, the energy levels of the two spin states (parallel or anti-parallel to the field) of a spin 1/2 particle split. At thermal equilibrium the polarization is given by the Curie law, $P = \tanh(\mu B/kT)$, where $\mu$ is the magnetic moment of the particle and $k$ the Boltzmann constant. In a magnetic field of 2.5 T and at a temperature below 1 K, due to their large magnetic moment, the electrons from the paramagnetic centers are nearly 100% polarized. On the other hand, the nuclear magnetic moments are much smaller and the resulting polarization of the nuclei is very small.
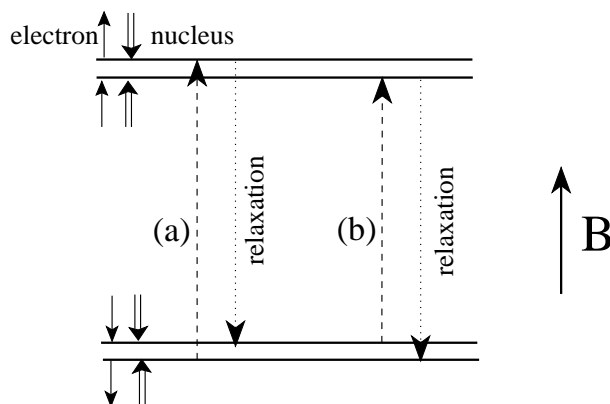


Figure 3.1: The energy levels of the coupled system made of a paramagnetic electron and a nearby nucleus.

DNP consists in transferring the electron polarization to the nuclei. The energy levels of the coupled system made of a paramagnetic electron and a nearby nucleus are presented in Fig. 3.1. At thermal equilibrium, the population is essentially spread equally over the two lower levels while the two upper levels are empty ($P_e \approx 100\%$ and $P_N \approx 0$). A microwave field is applied with a frequency corresponding for instance to transition ($a$) [1]. Because of its large magnetic moment the electron returns back to its equilibrium state within milliseconds (relaxation). The net effect is a negative polarization of the nucleus. Using a frequency which corresponds to transition ($b$) results in a positive polarization. This provides a polarization of the nuclei which are close to a paramagnetic center. The polarization then spreads over all nuclei in the material due to the dipolar coupling between nuclei.

The polarized target (Fig. 3.2) was equipped with two 60 cm long cells, polarized in op-

---

[1]For a free electron proton system we have the pure eigen-state of Fig. 3.1 and transition ($a$) corresponds to a simultaneous spin flip of the electron and the proton, which is forbidden. The coupling of the system produces a mixing of the eigen-states which makes the transition possible with a small probability.
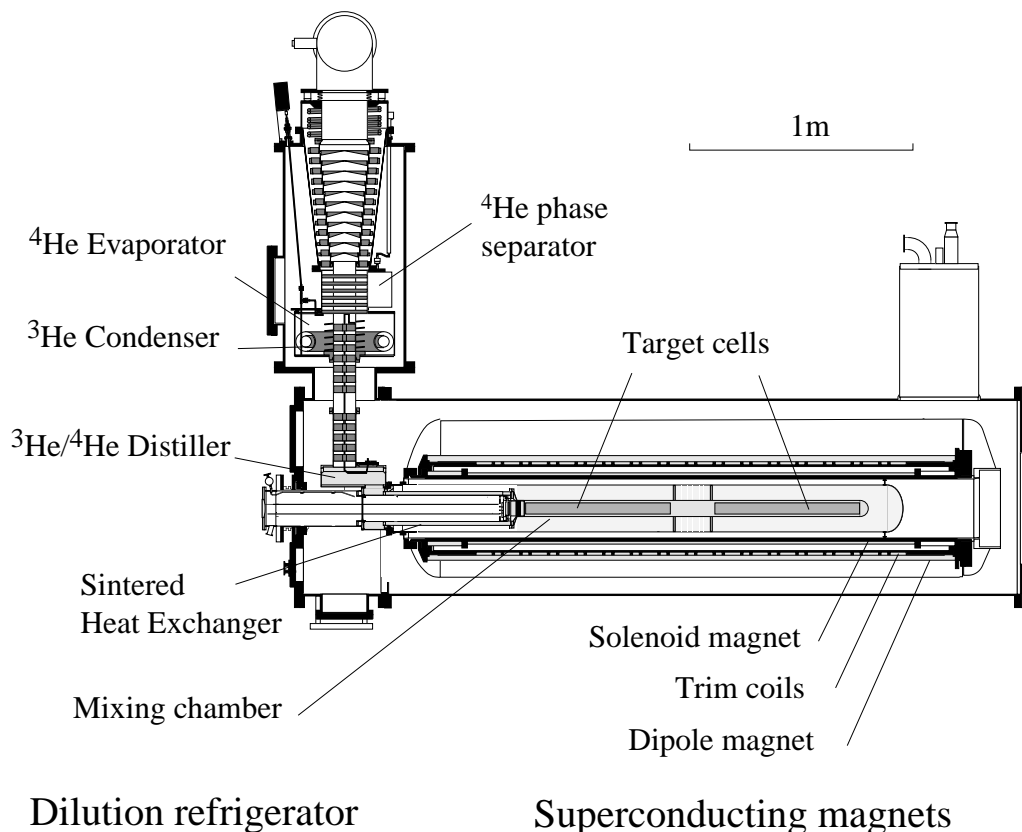
Figure 3.2: Cross section of the SMC polarized target.

posite directions. The cells were located in the mixing chamber of a $^3$He-$^4$He dilution refrigerator which cooled down the target material below 0.5 K during DNP process. When DNP was stopped temperatures below 50 mK were reached. In this *frozen spin* mode the relaxation time of the nuclear polarization exceeds 1000 hours. A superconducting solenoid magnet provided a 2.5 T field parallel to the beam and a system of 16 correction coils allowed for an homogeneity of $\pm 3.5 \times 10^{-5}$ over the target volume, which is needed for DNP. The 26.5 cm inner diameter of the solenoid magnet corresponds to an opening angle of 65 mrad as seen from the upstream end of the target. A superconducting dipole provided a 0.5 T field perpendicular to the beam. This allowed for a reversal of the spins without re-polarizing: the target was put in frozen spin mode and the dipole and solenoid field were varied in such a way that their vector sum rotated by 180$^o$ and the nuclear spins followed this rotation. The polarization was measured with 5 NMR coils in each cell with a relative accuracy of 3%. These measurements were calibrated through the measurement of the thermal equilibrium signal at 1 K, when the polarization is known from Curie law.

In order to control the superconducting magnets and the dilution refrigerator we used CPUs located in VME crates and connected to a workstation which provided graphical user interface [37]. This resulted in user friendliness, high reliability and flexibility. The system allowed for control, acquisition, display, storage, and for alarm generation. In

particular the rotation of the field was fully automated, as illustrated in Fig.3.3. It was then possible to perform it 5 times per day, loosing only 10 mn of data taking time and less than 0.2% polarisation.

However, at the beginning, an important loss of negative polarization was observed during the rotation and ascribed to the so-called *super radiance effect* [38]. This could be avoided by degrading the field homogeneity by intentionally mis-tuning the correction coils before the rotation. This modification could immediately be included in the automatic rotation procedure, which illustrated the flexibility of the system.
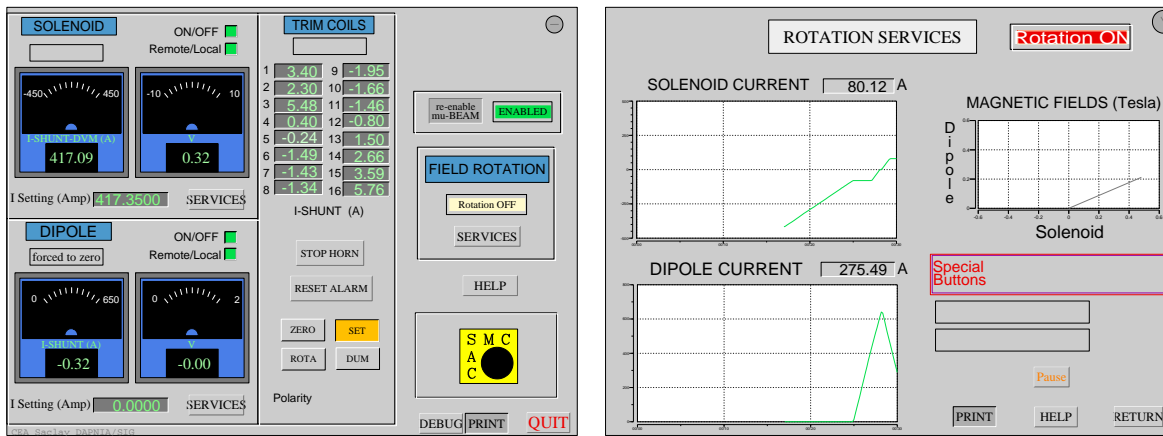


Figure 3.3: Polarized target magnet control. The left side shows the main control screen which displays information on all magnets (solenoid, dipole and trim coils). The trim coils can be operated from this screen, while clicking on the solenoid or dipole service button gives access to the corresponding control screens. Clicking on the field rotation service button gives access to the field rotation screen which is displayed on the right. The fully automatic rotation procedure is initiated by a single click. In the figure on the right the rotation has already started for some time. The solenoid current is being ramped from −416 to +416 A and the dipole is set on for the time when the solenoid current is small. The graph on the upper right side displays the vector sum of the 2 fields.

## 3.1.2   The spectrometer [7]

Fig. 3.4 presents a schematic view of the set-up. The incident muon track was determined in the beam definition section before the polarized target, using scintillating hodoscopes (BHA and BHB) and a MWPC (P0B). After interaction in the target the scattered muon and the produced hadrons were analyzed in the forward spectrometer which consisted in a 4.4 Tm dipole magnet (B8) surrounded by MWPC and drift chambers. The scattered muon was identified in a system of streamer tubes (ST67) and MWPCs (P67) located after a 2 m thick iron absorber. In total there were more than 100 planes of gaseous tracking
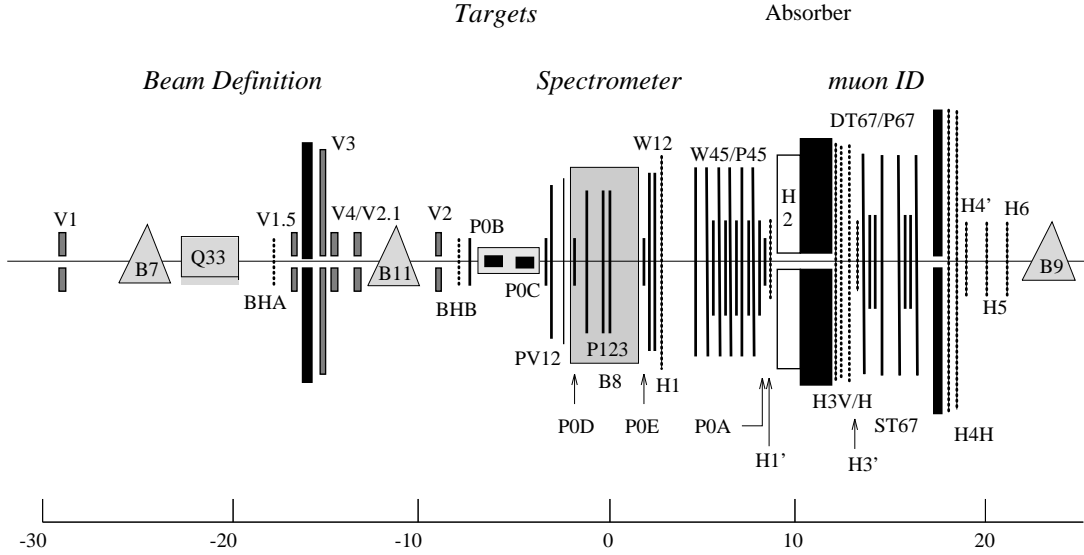
Figure 3.4: Schematic view of the SMC experimental set-up (see text).

detectors. Hadrons could be separated from electrons using the H2 calorimeter with an electromagnetic part which amounts to 20 radiation lengths followed by an hadronic part.

The data acquisition was triggered by coincidence matrices selecting patterns of hits in different planes of scintillator hodoscopes (H1, H3V, H3H and H4H). The matrices were tuned to select patterns compatible with a scattered muon (target pointing) and remove part of the triggers due to random coincidences or halo muons. The triggers were vetoed by veto counters (V1, V1.5, V3, V2.1, V2) surrounding the beam in the beam definition section, to further reduce the number of triggers due to halo muons.

### 3.1.3 The beam polarimeter

The muon beam is naturally polarized due to parity violation in the weak decay of the parent hadrons. For monochromatic muon and hadron beams, the polarization is a known function of the ratio $E_h/E_\mu$. For real muon and hadron beams the polarization can, in principle, be computed through a Monte Carlo simulation [39] of the beam line. However, some uncertainty arises in this calculation from the distribution of the parent hadrons, and the corresponding phase space over which the integration must be performed. The quoted relative error was 7.5%, which was making it one of the dominant errors of the EMC measurement. The SMC then decided to build a polarimeter to measure the beam polarization. Two different methods were used. The polarization was measured through the energy spectrum of positrons from muon decay, $\mu^+ \to e^+ \bar{\nu}_\mu \nu_e$ (decay method), and through double spin asymmetry in elastic muon-electron scattering (asymmetry method).
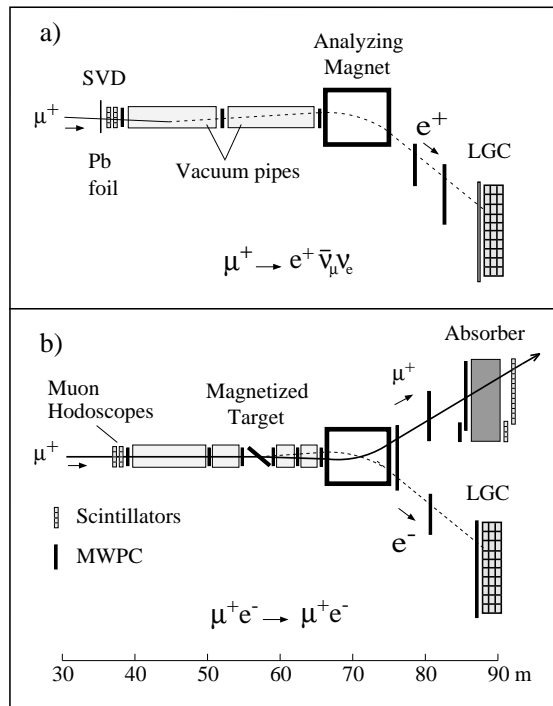
Figure 3.5: Schematic view of the beam polarimeter for the decay method (a) and the asymmetry method (b).

**The decay method [40, 41]**

In the muon center of mass frame the decay positron is preferentially produced parallel to the spin of the muon. After Lorenz boost to the laboratory frame, this results in a dependence of the positron energy spectrum (the so-called Michel spectrum) on the polarization, as illustrated in the insert of Fig. 3.6. The setup for the decay method is presented in Fig. 3.5-a. Muons could decay inside a 30 m long vacuum pipe. The resulting positrons were analyzed in a magnetic spectrometer and identified in a lead glass calorimeter (LGC). Positrons from decay which occurred upstream of the vacuum pipe were vetoed by a shower veto detector (SVD) consisting of a lead foil followed by two scintillator hodoscopes. The measured positron energy spectrum had to be corrected by the polarimeter acceptance, which had to be carefully estimated by a MC simulation.

The MC simulation requires a beam file as input. In 1996 it was realized that the correction related to the inter-calibration between the beam momentum station and the polarimeter analyzing magnet was missing in this beam file. After correction the result was found not to be compatible any more with the MC expectation and the result of the asymmetry method. In addition it appeared that the result was not stable versus the cuts. This triggered a new and important effort on the topic, by people not originally involved. We realized that the analysis was much more delicate than for the asymmetry method, where many systematic effects cancel in the asymmetry. Since the decay

method involves the measurement of the shape of an energy spectrum, it relies heavily on the MC simulation, which has to be excellent. All steps were reevaluated: several bugs were found; the alignment was improved; the effect of the residual background was studied; leading to a re-evaluation of the systematic error which had to be increased; and a careful study of all cuts was performed in order to improve the comparison between data and MC simulation. In particular the positron identification cut in the LGC had to be tightened and combined with some geometrical cuts to remove the class of events for which a reliable simulation was not possible. Finally, after several months of work, a stable situation was obtained. The agreement of the data after MC acceptance correction with the Michel spectrum is illustrated in Fig. 3.6. The result of the fit over the indicated range is $P_\mu = -0.806 \pm 0.013 \pm 0.026$ for $E_\mu = 187.4$ GeV.
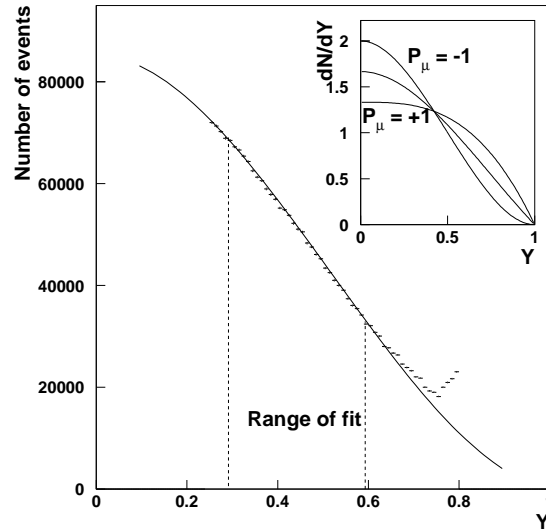


Figure 3.6: Experimental decay positron energy spectrum after acceptance correction compared to the Michel spectrum for $P_\mu = -0.806$. The two vertical dashed lines indicate the range of the fit. The dependence of the Michel spectrum upon polarization is illustrated in the insert.

## The asymmetry method [41]

The measured elastic muon-electron scattering asymmetry, $A_{exp}$, is related to the physics asymmetry, $A_{\mu e}$, by $A_{exp}(y_{\mu e}) = P_e P_\mu A_{\mu e}(y_{\mu e})$, where $P_e$ is the electron polarization. The physics asymmetry $A_{\mu e}$ is known precisely from QED. So once $P_e$ is known, the measurement of $A_{exp}$ in each bin in $y_{\mu e}$ provides an independent measurements of $P_\mu$. The setup (Fig. 3.5-b) is different from the decay method setup. The polarity of the analyzing magnet is inverted and a second telescope is installed after the magnet. The knocked out electron and the scattered muon are identified in the LGC and in a scintillating counter hodoscope after a 2 m thick iron absorber, respectively. The polarized electron target is made of a 49% Fe, 49% Co and 2% V ferromagnetic alloy. The total magnetization of the

target is measured with a pick-up coil. It is principally due to spins but it also includes a small contribution due to orbital momentum, $M = M_S + M_0$. To obtain $M_S$ and the corresponding electron polarization it is assumed that $M_S/M$ for our alloy is the same as for 50% Fe, 50% Co alloy which is known [2]. The target field orientation was inverted between SPS pulses and the target angle with respect to the beam was changed between $+25\%$ and $-25\%$ every hour to cancel systematic effects due to the target field.

Backgrounds, due to pair production and to bremsstrahlung followed by conversion, were strongly reduced by applying cuts corresponding to 2 body kinematics. After cuts, radiative corrections to the asymmetry are smaller than 1% over the full range of $y_{\mu e}$. The results of all bins are compatible and they average to $P_\mu = -0.797 \pm 0.011 \pm 0.012$ for $E_\mu = 187.4$ GeV. This is in good agreement with the decay result, $P_\mu = -0.806 \pm 0.013 \pm 0.026$, and the MC prediction, $P_\mu = -0.79 \pm 0.04$, which validates a posteriori the MC simulation[3].

## 3.2    Inclusive analysis

Deuteron data were taken in 1992, 1994 and 1995 with a deuterated butanol target. Proton data were taken in 1993 with a butanol target and in 1996 with an ammonia target, which provides a better dilution factor than butanol. For most of the data the beam energy was 190 GeV and the following cuts were applied, $\nu = E - E' > 15$ GeV, $y = \nu/E < 0.9$, $p'_\mu > 19$ GeV and $\theta_\mu > 9$ mrad.

### 3.2.1    Extraction of asymmetries [7]

Asymmetry extraction was the topic of many studies. Here we present the main results. The derivations and some more results can be found in Compass note 2004-03 added in addendum.

The numbers of muons $N_u$ and $N_d$ scattered in the upstream and downstream target cells, respectively, are given by

$$N_u = \Phi\, n_u a_u \sigma (1 - f P_\mu P_u A_\parallel) \quad \text{and} \quad N_d = \Phi\, n_d a_d \sigma (1 - f P_\mu P_d A_\parallel), \qquad (3.1)$$

where $\Phi$ is the integrated beam flux, $n_u$ and $n_d$ the area densities of the two target nucleon cells, $a_u$ and $a_d$ the corresponding spectrometer acceptances, $\sigma$ the unpolarized cross section, $f$ the dilution factor which accounts for the fact that only a fraction of the target nucleons is polarized, $P_u$ and $P_d$ the polarizations in the two target cells, and $A_\parallel$ the

---

[2]As for $M$ we have for the kinetic moment is $J = J_S + J_0$. The relation between $M$ and $J$ are different for the spin, $M_S/J_S = g_e(e/2mc)$, and the orbital momentum contributions, $M_0/J_0 = (e/2mc)$. So by experimentally measuring $M/J$ in an Einstein-de Haas experiment one can determine the fractions of spin and orbital momentum contributions to $M$ and the required $M_S/M$.

[3]Between the EMC and the SMC times the MC of the beam line was improved, reducing the quoted error from 0.06 (7.5%) to 0.04.

cross section asymmetry for longitudinally polarized target. As detailed in section 2.2.2, $A_\parallel$ is related to the virtual photon asymmetry by $A_\parallel = DA_1$, where $D$ is the depolarisation factor.

## Standard method

The flux $\Phi$ and the spin-independent cross-section $\sigma$ cancel in the evaluation of the raw counting-rate asymmetries, $A_{\mathrm{RAW}}$ and $A'_{\mathrm{RAW}}$, obtained before and after target polarization reversal:

$$A_{\mathrm{RAW}} = \frac{N_{\mathrm{u}} - N_{\mathrm{d}}}{N_{\mathrm{u}} + N_{\mathrm{d}}}, \qquad A'_{\mathrm{RAW}} = \frac{N'_{\mathrm{d}} - N'_{\mathrm{u}}}{N'_{\mathrm{d}} + N'_{\mathrm{u}}}. \tag{3.2}$$

Provided that $r = n_{\mathrm{u}} a_{\mathrm{u}} / n_{\mathrm{d}} a_{\mathrm{d}}$ is the same before and after polarization reversal and close to unity [4], the acceptances $a$ and the densities $n$ cancel in the average of the raw asymmetries and $A_1$ is given by

$$A_1 = -\frac{1}{f D P_\mu P_{\mathrm{t}}} \left[ \frac{A_{\mathrm{RAW}} + A'_{\mathrm{RAW}}}{2} \right], \tag{3.3}$$

where $P_{\mathrm{t}}$ is the weighted average of the target cell polarizations. If, however, $r$ changes after reversal and becomes $r' \neq r$ a 'false' asymmetry appears,

$$A_{\mathrm{false}} = -\frac{1}{2 f D P_\mu P_{\mathrm{t}}} \left[ \frac{r-1}{r+1} - \frac{r'-1}{r'+1} \right]. \tag{3.4}$$

## Weighted method

Equation (3.3) is not optimal from a statistical point of view because it gives the same weight to all events, independently of how much information they carry on the asymmetry. This depends on $f D P_\mu$ and then on event kinematics. A *weighted method* was developed, where each event is weighted by its individual weight, $w = f D P_\mu$ , and the asymmetry is obtained as

$$A_1 = -\frac{1}{2 P_{\mathrm{t}}} \left[ \left( \frac{\sum w_{\mathrm{u}} - \sum w_{\mathrm{d}}}{\sum w_{\mathrm{u}}^2 + \sum w_{\mathrm{d}}^2} \right) + \left( \frac{\sum w_{\mathrm{d}} - \sum w_{\mathrm{u}}}{\sum w_{\mathrm{d}}^2 + \sum w_{\mathrm{u}}^2} \right)' \right], \tag{3.5}$$

where $\sum$ indicates a sum over the events. The statistical error is then

$$\delta A_1 = -\frac{1}{2 P_{\mathrm{t}}} \sqrt{\left( \frac{1}{\sum w_{\mathrm{u}}^2 + \sum w_{\mathrm{d}}^2} \right) + \left( \frac{1}{\sum w_{\mathrm{d}}^2 + \sum w_{\mathrm{u}}^2} \right)'}. \tag{3.6}$$

which is smaller that the error obtained using Eq. (3.3) by a factor $\langle w^2 \rangle / \langle w \rangle^2 = 1 + \sigma_w^2 / \langle w \rangle^2$, where $\sigma_w^2$ is the variance of the weight. The larger $\sigma_w / \langle w \rangle$, the larger the gain in statistics with the weighted method.

---

[4] actually a workaround can be found if $r$ is far from unity, as explained in the note in addendum.

Any quantity which depends only on the event kinematics can be included in the weight but one should not include a time dependent quantity like $P_T$. In this case the cancellation of the acceptance would not be warranted any more and important false asymmetries could appear. This is what happened in a first analysis of transverse asymmetries. In transverse mode $P_T$ is regularly decreasing with time because polarization by DNP cannot be applied with the transverse magnetic field. This first analysis was giving large negative transverse asymmetries at small $x$ which disappeared when $P_T$ was removed from the weight, as shown in Fig. 3.7.
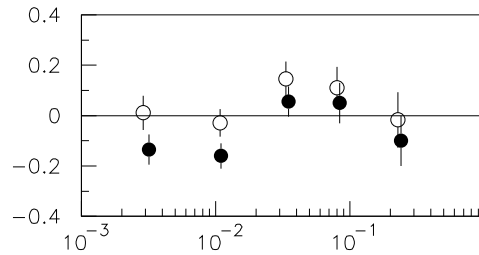


Figure 3.7: Results of the first analysis of $A_2$ (full circles) and published results (open circles).

## 3.2.2 Radiative corrections

In the first SMC analysis the radiative corrections were not properly applied. This is detailed in SMC note 96/09 added in addendum where a correct procedure is also described. Here we give a short description of the correct procedure.

QED radiative corrections (see section 2.1.5) are applied to convert the measured asymmetries (Eq. 3.5) to one-photon exchange asymmetries. These corrections are calculated using:

$$\overline{\sigma}^{\mathrm{T}} = v\overline{\sigma}^{1\gamma} + \overline{\sigma}_{\mathrm{tail}}, \qquad \Delta\sigma^{\mathrm{T}} = v\Delta\sigma^{1\gamma} + \Delta\sigma_{\mathrm{tail}}, \tag{3.7}$$

where $\overline{\sigma}^{\mathrm{T}}$ is the total, i.e. measured, spin-independent cross-section, $\overline{\sigma}^{1\gamma}$ is the corresponding one-photon exchange cross-section, and $\overline{\sigma}_{\mathrm{tail}}$ is the contribution to $\overline{\sigma}^{\mathrm{T}}$ from the elastic, the quasi-elastic and the inelastic radiative tails. The corresponding differences of cross sections, for anti-parallel and parallel orientations of lepton and target spins, are denoted by $\Delta\sigma$. The factor $v$ accounts for virtual radiative corrections and also includes the effect of the emission of real photons of low energy (low enough so that the event remains in a given $x$ bin). By varying the size of the bin, one can move contributions from the inelastic radiative tail to the factor $v$. The decomposition in Eq. 3.7 is therefore to some extent ambiguous. Using the program TERAD [42] we find $0.98 < v < 1.03$ in the kinematic range of our data. For simplicity we set $v$ to unity in our analysis and attribute all corrections to $\sigma_{\mathrm{tail}}$.

Neglecting $A_2$ and thus implying $A_1 = \Delta\sigma/(2D\sigma)$, the radiative corrections to the one-photon asymmetry, $A_1^{1\gamma}$, can be written as

$$A_1^{\mathrm{T}} = \rho(A_1^{1\gamma} + A_1^{\mathrm{rc}}), \qquad (3.8)$$

with $\rho = v\,\overline{\sigma}^{1\gamma}/\overline{\sigma}^{\mathrm{T}}$ and $A_1^{\mathrm{rc}} = \Delta\sigma_{\mathrm{tail}}/2vD\overline{\sigma}^{1\gamma}$.

The ratio $\overline{\sigma}^{1\gamma}/\overline{\sigma}^{\mathrm{T}}$ and the correction $A_1^{\mathrm{rc}}$ are evaluated using the program POLRAD [43]. The asymmetry $A_1(x)$ required as input to compute $A_1^{\mathrm{rc}}$ is a fit from SMC and SLAC data available at the time of the analysis. The contribution from $A_2^{\mathrm{p}}$ is neglected. The uncertainty in $A_1^{\mathrm{rc}}$ is estimated by varying the input values of $A_1$ within the errors.

We have incorporated $\rho$ into the evaluation of the dilution factor, $f' = \rho f$, on an event-by-event basis. Using the weight $w = f'DP_\mu$, Eq. (3.5) directly provides $A_1^{\mathrm{T}}/\rho$ and then, using Eq. (3.8), $A_1^{1\gamma}$.

The probability to emit a real photon decreases as $1/E_\gamma$. Therefore the inelastic radiative tail from a given $x$ bin quickly decreases when going to lower and lower $x$. The situation is different for the elastic and quasi elastic tails. When going to lower $x$ we are sensitive to the radiative tail from lower $Q^2$ and the elastic cross section increases rapidly when going to lower $Q^2$, in such a way that the elastic radiative tail actually increases at low $x$ and $\rho$ becomes significantly smaller than 1. The first analysis was giving nearly correct values of the asymmetries, but the statistical errors were underestimated by a factor up to 1.4 at $x = 0.005$ ! This was due to assuming $\delta A_1^{1\gamma} = \delta A_1^{\mathrm{T}}$ instead of $\delta A_1^{1\gamma} = (1/\rho)\delta A_1^{\mathrm{T}}$.

We found out that the same problem was present in the analysis of the NMC unpolarized data. We had to convince our NMC colleagues and they made the required corrections just before publication.

### 3.2.3 Hadron-tagged method [22]

As explained above the elastic radiative tail contribution is large at low $x$, which degrades the statistical resolution. This radiative tail contribution can be removed by including in the analysis only events where a charged hadron was measured. This is the so-called hadron-tagged method. At low $x$, $W$ is large and MC simulations show that for $x < 0.02$ the fraction of DIS events removed by hadron tagging ranges between 2 and 7% and the method provides a net gain in statistical accuracy. At high $x$ the fraction of DIS events removed is larger and the elastic radiative tail is anyway small. MC simulation also showed that the method does not introduce any bias on the measured asymmetry at low $x$. So the hadron-tagged method is used for $x < 0.02$ and the standard inclusive method is used for larger $x$.

### 3.2.4 Results [22]

The measured $A_\parallel$ asymmetry is related to the virtual photon asymmetry by $A_\parallel = D(A_1 + \eta A_2)$ and using Eqs. (2.16) one can write $g_1 = F_1(A_1 + \gamma A_2)$. In SMC kinematics $\eta$ and

$\gamma$ are small and the asymmetries $A_2^p$ and $A_2^d$ measured by SMC are compatible with zero. So the $A_2$ term was neglected and its possible contribution was included in the systematic errors.
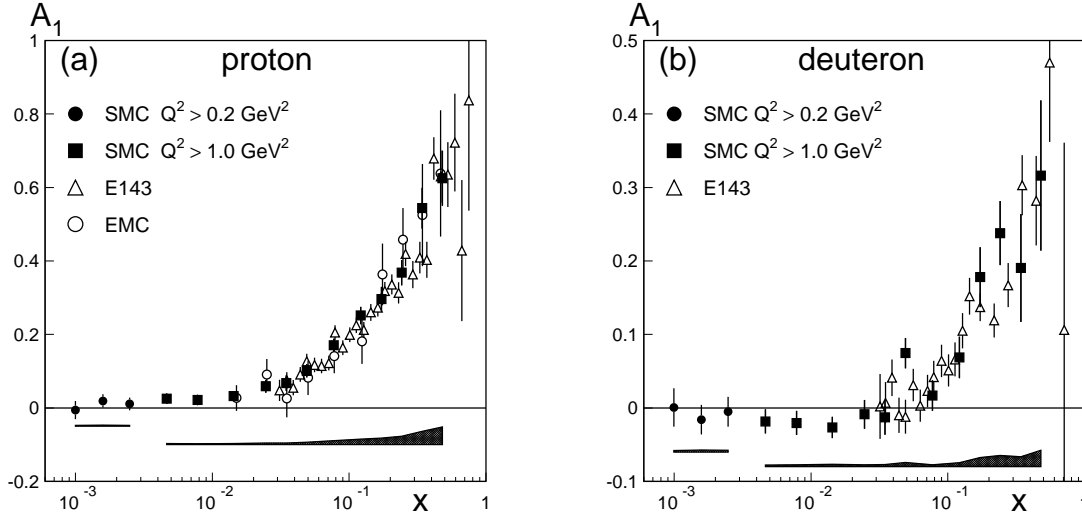


Figure 3.8: $A_1$ asymmetries measured by SMC for proton (left) and deuteron (right) together with other results available at the time of publication from EMC and E143. Statistical errors are shown as error bars while the shaded bands below indicate the systematic uncertainty of the SMC measurement.

The final $A_1$ asymmetries measured by SMC are presented in Fig. 3.8. Contributions to systematic errors include false asymmetries and uncertainties on target and beam polarizations, dilution factor, radiative corrections, $A_2$ contributions and $R$. The statistical errors of SMC data are much smaller than EMC and they extend to lower $x$. The statistical errors of E143 at SLAC are even smaller but their data do not extend to as low $x$, which is very important for the extrapolation and the extraction of the first moments.

The structure function $g_1$ obtained from the measured $A_1$ using $g_1 = F_1 A_1 = F_2 A_1/(2x(1+R))$ is presented in Fig. 3.9. All $g_1$ data at $Q^2 > 1$ GeV$^2$ are evolved to $Q_0^2 = 10$ GeV$^2$ using $g_1(x, Q_0^2) = g_1(x, Q^2) + \left[ g_1^{\text{fit}}(x, Q_0^2) - g_1^{\text{fit}}(x, Q^2) \right]$ where $g_1^{\text{fit}}$ is the fit of $g_1$ resulting from the NLO QCD analysis [23] presented in the next section. The integrals over the measured $x$ range give

$$\int_{0.003}^{0.7} g_1^p(x, Q_0^2 = 10)dx = 0.131 \pm 0.005 \pm 0.006 \pm 0.004 \qquad (3.9)$$

$$\int_{0.003}^{0.7} g_1^d(x, Q_0^2 = 10)dx = 0.037 \pm 0.006 \pm 0.003 \pm 0.003 \qquad (3.10)$$

where the first error is statistical, the second systematic and the third is due to the uncertainty in the $Q^2$ evolution. Adding the contributions to the integrals from the unmeasured range in $x$, estimated from the QCD fit, we get

$$\int_0^1 g_1^p(x, Q_0^2 = 10)dx = 0.120 \pm 0.005 \pm 0.006 \pm 0.014 \qquad (3.11)$$
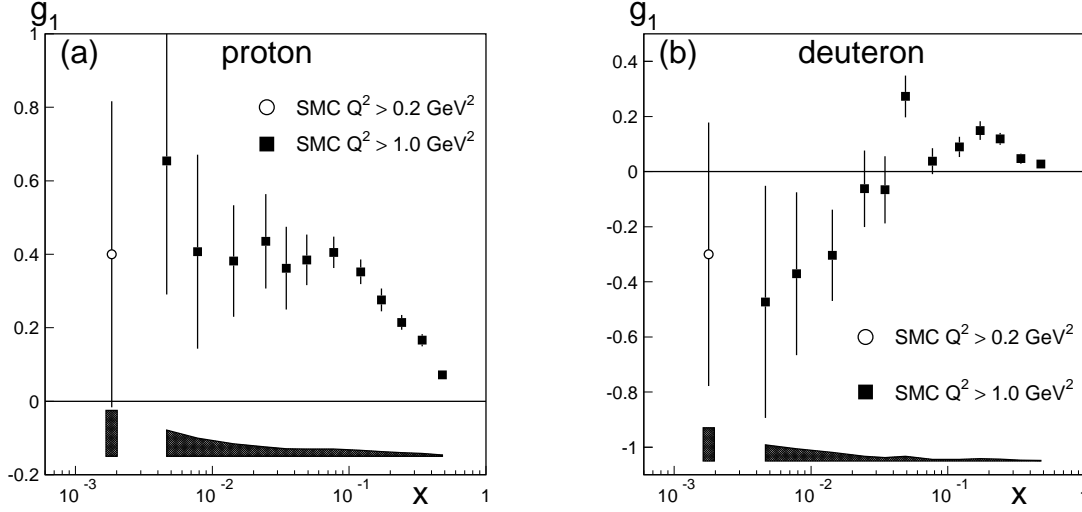
Figure 3.9: The $g_1$ structure function measured by SMC for proton (left) and deuteron (right). Statistical errors are shown as error bars while the shaded bands below indicate the systematic uncertainty of the SMC measurement. The single point at $Q^2 > 0.2$ was obtained by combining the three $A_1$ bins at $Q^2 > 0.2$ in Fig 3.8.

$$\int_0^1 g_1^d(x, Q_0^2 = 10)dx = 0.019 \pm 0.006 \pm 0.003 \pm 0.013. \tag{3.12}$$

where the last error now also includes the error in the low $x$ and high $x$ extrapolations. This is far below the Ellis-Jaffe predictions (Eq. 2.23) at $Q^2 = 10$ GeV$^2$, $\Gamma_1^p = 0.170 \pm 0.004$ and $\Gamma_1^d = 0.071 \pm 0.004$.

## 3.2.5 QCD analysis [23]

All $g_1$ data available were used to perform a NLO QCD analysis using NLO polarized Wilson coefficients and splitting functions (see section 2.2.4). The polarized pdf's are parametrized at $Q^2 = 1$ GeV$^2$ as $\Delta f = N \eta_f x^{\alpha_f}(1-x)^{\beta_f}(1+a_f x)$, where $\int N(\eta_f, \alpha_f, a_f)$ is a normalization factor such that $\int_0^1 \Delta f(x)dx = \eta_f$. The NS normalizations are fixed by $\eta_{NS}^{p,n} = \pm \frac{3}{4}\frac{g_A}{g_V} + \frac{1}{4}a_8$. The $\Delta f$ are evolved to the $Q^2$ of the data using the DGLAP equations (Eqs. 2.19 and 2.20), they are used to compute $g_1$ according to Eqs. (2.18), the result is compared to the data to compute a $\chi^2$, and the parameters are varied in order to minimize this $\chi^2$. The resulting pdf's are shown in Fig. 3.10. The theoretical uncertainty includes uncertainties on factorization and renormalization scales, on $\alpha_s$, on the quark mass threshold and on $g_A/g_V$. We get for the integral over x:

$$\Delta g(1\text{GeV}^2) = 0.99 \, ^{+1.17}_{-0.31} \, (\text{sta.}) \, ^{+0.42}_{-0.22} \, (\text{sys.}) \, ^{+1.43}_{-0.45} \, (\text{th.}) \tag{3.13}$$

and $a_0 = 0.19 \pm 0.05 \pm 0.04$. In order to test the Bjorken sum rule the value of $g_A/g_V$ must be set free, which gives at $Q^2 = 5$ GeV$^2$:

$$\Gamma_1^p - \Gamma_1^n = 0.174 \, ^{+0.005}_{-0.005} \, (\text{sta.}) \, ^{+0.011}_{-0.009} \, (\text{sys.}) \, ^{+0.021}_{-0.006} \, (\text{th.}) = 0.174 \, ^{+0.024}_{-0.012} \,, \tag{3.14}$$

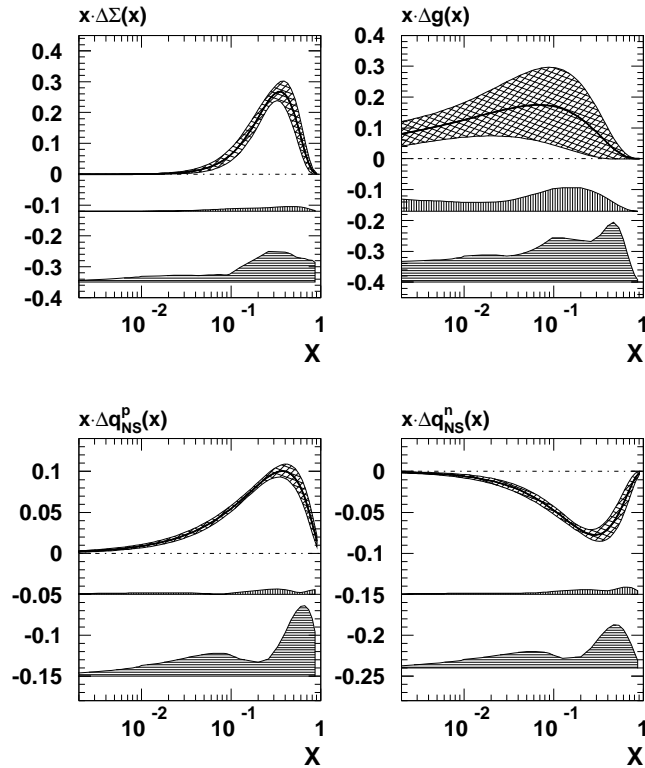in good agreement with the theoretical prediction $\Gamma_1^p - \Gamma_1^n = 0.181 \pm 0.003$.

Figure 3.10: Polarized parton distributions at $Q^2 = 1$ GeV$^2$ obtained by the SMC from the QCD NLO analysis of SMC, SLAC and Hermes $g_1$ data. The statistical error is shown by a band with crossed hatch. The experimental systematic and theoretical uncertainty are shown by the vertically and horizontally hatched bands, respectively.

## 3.3  Semi-inclusive analysis

Spin asymmetries in semi inclusive data, $l + p \rightarrow l + h + X$, were studied [44]. The same kinematical cuts as in the inclusive analysis were applied and in addition $z = E_h/\nu > 0.2$ was required. The ratio of the energy deposited in the electromagnetic part of the H2 calorimeter to the total deposited energy exhibits a peak near 1, which corresponds to electrons. To get a clean hadron sample, electrons were removed by requiring this ratio to be smaller than 0.8.

Semi inclusive asymmetries were used to extract polarized quark pdf's as explained in section 2.3. The strange fragmentation functions to pions, $D_{s,\bar{s}}^{\pi^-,\pi^+}$, was assumed to equal the disfavored fragmentation function, $D_u^{\pi^-}$ (e.g. the probability to produce a $\bar{u}d$ from a $s$ is the same as from a $u$). Due to limited statistics the additional assumption $\Delta\bar{u} = \Delta\bar{d} = \Delta s = \Delta\bar{s} \equiv \Delta\bar{q}$ was needed. The hadron sample contains mainly $\pi$, so $\Delta s$ always enters together with a disfavored fragmentation function, $\Delta\bar{q}$ provides essentially information on the non-strange sea quarks and the assumption on $\Delta s$ and $\Delta\bar{s}$ has a negligible influence on the result.

In this analysis one must take into account the statistical correlations between the different asymmetries. In the first analysis these correlations were wrong. We re-derived them carefully. The derivations and the results appear in COMPASS note 2004-4 included in Addendum. We have for instance $\rho(A, A_h) = \langle n_h \rangle / \sqrt{\langle n_h^2 \rangle}$.

The polarized pdf's obtained by SMC are presented in Fig. 3.11. We note that the polarized $u$ valence quark distribution, $\Delta u_v(x)$, is positive, the polarized $d$ valence quark distribution, $\Delta d_v(x)$, is negative and the non-strange sea distribution, $\Delta \bar{q}$, is compatible with zero. The integral are $\int_0^1 \Delta u_v(x) dx = 0.77 \pm 0.10 \pm 0.08$, $\int_0^1 \Delta d_v(x) dx = -0.52 \pm 0.14 \pm 0.09$ and $\int_0^1 \Delta u_v(x) dx = 0.01 \pm 0.04 \pm 0.03$. Hermes results, which came later, have smaller statistical errors but they do not cover as low $x$ as SMC.
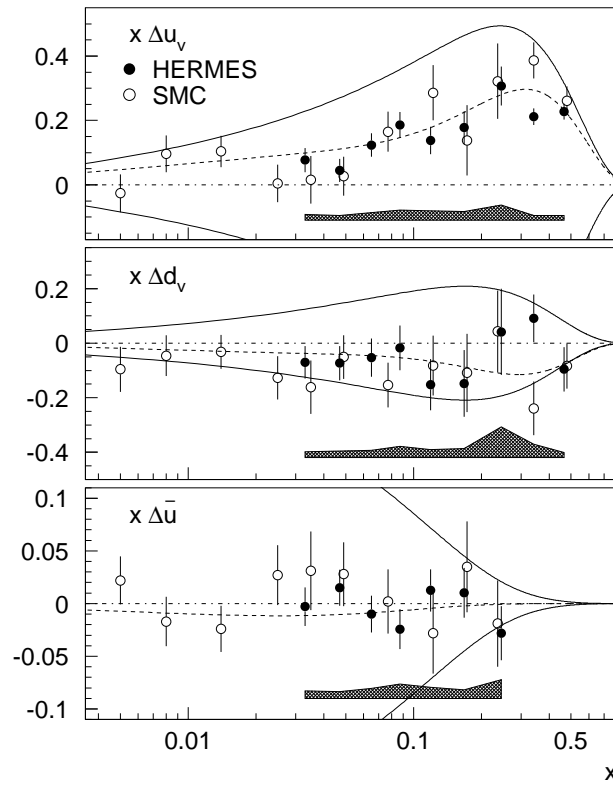


Figure 3.11: Polarized quark distribution functions measured by the SMC and Hermes collaborations in semi inclusive analysis.

## 3.4 Conclusions

The SMC experiment confirmed the violation of the Ellis-Jaffe sum rule observed by the EMC and provided the first check of the Bjorken sum rule. The result quoted by EMC is $\Gamma_1^p = 0.123 \pm 0.013 \pm 0.019 \pm 0.003$ while SMC gets $\Gamma_1^p = 0.120 \pm 0.005 \pm 0.006 \pm 0.014$. SMC improved a lot relative to EMC on statistical and experimental systematic errors. However, it was realized that the theoretical error on the first moment, related in

particular to the low $x$ extrapolation, was as large as 0.014 to be compared to the "naive" assumption of 0.003 of EMC, based on Regge theory.

Results obtained for $g_1$ at SLAC [24] and later at DESY [25] are compatible with the SMC results. So the EMC result is clearly confirmed from the experimental point of view. The interpretation in terms of the fraction $\Delta\Sigma$ of the nucleon spin carried by the spin of the quark is delicate. It depends on what is assumed for the gluon spin contribution.

This triggered a new generation of experiments aiming at a direct measurement of the gluon polarization inside the nucleon: COMPASS at CERN, experiments at Brookhaven/RHIC and E162 at SLAC. The next chapter will focus on COMPASS.

# Chapter 4

# The COMPASS experiment

The COMPASS experiment [45] was set up with the main objective of measuring the gluon polarization in the nucleon, $\Delta g/g$ (section 2.5). It aims also at a measurement of transversity (section 2.4) and several other measurements with a polarized muon beam. In addition there is a full program of measurements with the same set up but using hadron beams.

## 4.1   Experimental set up

The measurement of open charm puts strong constraints on the experimental apparatus. The cross sections are small and we want to measure asymmetries, so a high luminosity is required. Due to the multiple scattering in the thick polarized target, it is not possible to separate the $D^0$ decay vertex from the main DIS vertex and the $D^0$ can only be identified by its invariant mass. Therefore, in order to single out the $D^0 \to K\pi$ channel, one needs a good mass resolution (and of course a good $K$ identification). This requires detectors with good resolution and a low mass to minimize multiple scattering.

The COMPASS experiment is installed in the same hall as SMC. The M2 high energy muon beam line was upgraded to $2 \times 10^8$ muons per 5 s spill every 16.8 s. The result of the MC simulation of the beam-line in terms of polarization was validated by the SMC beam polarization measurements (section 3.1.3). So the simulation is used for COMPASS. It gives an average polarization of 76% for the 160 GeV beam.

Fig. 4.1 gives an overall view of the set-up, which includes two successive spectrometers. The Large Angle Spectrometer (LAS) is dedicated to low-momentum large-angle particles, while the Small Angle Spectrometer (SAS) covers small angles and high momenta. Both include a Spectrometer Magnet (SM1 and SM2) surrounded by tracking detectors, electromagnetic and hadronic calorimeters and some absorbers followed by trackers for muon identification (muon filter). The LAS is equipped with a RICH detector to identify $K$. Due to financial and manpower constraints, the possibility to build a second RICH to

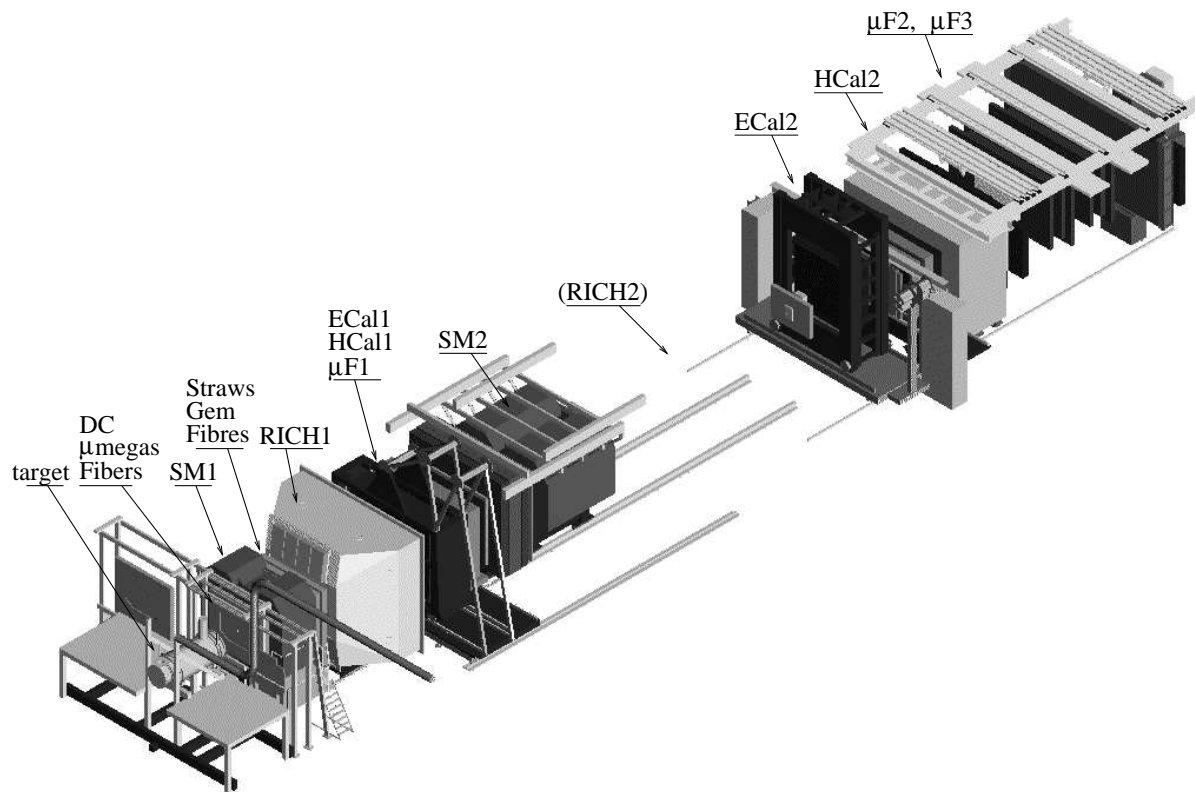equip the SAS was postponed to a latter upgrade.



Figure 4.1: Schematic view of the COMPASS set-up.

The SMC dilution refrigerator is used for the polarized target. A new superconducting magnet with a large bore, giving 180 mrad acceptance from the upstream end of the target cell, was designed. It is unfortunately not yet operational and the SMC magnet with only 60 mrad acceptance is used for the moment. This implied an unforeseen and delicate re-installation of the SMC magnet itself and of the control system described in section 3.1.1. Due to license issues an old version of Unix had to be re-installed with the proper network parameters. Then the possibility to communicate between the magnet control and the other part of the target control had to be established. The reduced acceptance of the SMC magnet has, however, a limited impact on the physics, as discussed below. The target is equipped with two 60 cm long cells, polarized in opposite directions. The target materials are $^6$LiD as deuterium target and $NH_3$ as proton target. $^6$Li can be described as a spin zero $^4$He, together with a quasi deuterium, so the naive dilution factor is very large, 4/8=0.5.

The tracking between the polarized target and the first magnet SM1 is under Saclay responsibility. This is the hottest region, since after SM1 low energy particles produced in the target are swept away. Due to the fast variation of the particle flux with the

distance from the beam, the tracking had to be split in three zones. The beam area ($\phi$ up to $5 \times 10^7$ Hz/cm$^2$) is covered by $5 \times 5$ cm$^2$ scintillating fiber detectors built by another team. The small angle tracking ($\phi$ up to $3 \times 10^5$ Hz/cm$^2$) is performed by $40 \times 40$ cm$^2$ micromegas detectors [46] and the large angle tracking ($\phi$ up to $10^4$ Hz/cm$^2$) by $120 \times 120$ cm$^2$ drift chambers (DC). The micromegas detectors and the drift chambers exhibit excellent performances in spite of the very difficult environment. The micromegas average efficiency is 96% and their resolution 92 $\mu$m. The DC average efficiency is 97% and their resolution 220 $\mu$m.

COMPASS is the first high energy experiment to use the novel micromegas detector [47], developed in Saclay. Micromegas are gaseous detectors made of 3 parallel electrodes: a drift electrode, a micro-mesh and a micro-strip PCB (Fig. 4.2). The particles ionize the gas in the conversion gap between the drift electrode and the micro-mesh. In this region the electric field is typically 1500 V/cm and the electrons simply drift up to the mesh. Due to the configuration of fields the mesh is essentially transparent to the electrons which pass through it and enter the amplification gap between the micro-mesh and the PCB, where the field is 40 kV/cm. The electrons then get enough energy to ionize other atoms and initiate an avalanche. The resulting avalanche electrons are collected on the micro-strips. Due to the configuration of field the ions are collected on the micro-mesh and do not enter the conversion gap. The short drift distance for the ions provides a fast collection and a high rate capability. In contrast with standard micro-strips detectors, micromegas do not have the problem of ions being collected on insulating materials.
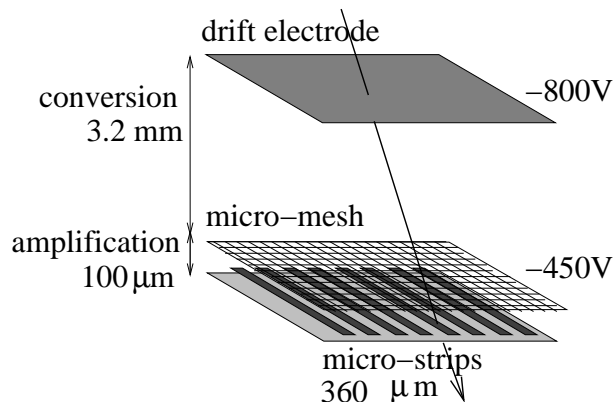


Figure 4.2: Schematic view of the COMPASS version of the micromegas detector. The active surface is $40 \times 40$ cm$^2$.

A similar splitting of the tracking exists after SM1, where the DCs are replaced by straw detectors and the micromegas by GEM detectors (Gas Electron Multiplier). The tracking in the SAS is based on GEMs and on MWPCs. Drift tube detectors are used in the first muon filter.

In a medium of refractive index $n$, particles with a velocity $\beta$ larger than $1/n$ produce photons with an angle such that $\cos \theta = 1/n\beta$. Ring Imaging Cherenkov detectors (RICH) are based on the measurement of this Cherenkov angle, which provides $\beta$ and then the mass of the particle if its momentum is known, allowing for particle identification. The

COMPASS RICH is filled with $C_4F_{10}$ with $n = 1.00153$, which corresponds to 2.5 and 8.9 GeV threshold for $\pi$ and $K$, respectively. The Cherenkov photons are reflected on UV mirrors toward photo sensitive detectors located on the focal plane of the mirrors, outside the acceptance. These detectors are wire chambers equipped with CSi photo-cathodes which convert the photons in electrons. The signal is read on 83,000 pads.

As in SMC, the data taking is triggered by coincidences between 2 planes of scintillator hodoscopes and vetoed by veto counters surrounding the beam. A dedicated trigger was designed to cover the very low $Q^2$. In this region the scattered muon is essentially at zero angle, but it separates from the beam due to its lower energy and the bending in SM1 and SM2. In addition a minimum energy deposit in the hadronic calorimeters has to be required for all triggers, except for the large $Q^2$ trigger.

## 4.2 Event reconstruction

COMPASS produces on the order of 20,000 triggers per spill with an average event size of 35 kB. This corresponds to a flux of 40 MB per second. The total amount of data is on the order of 300 TB per year. The data are stored on tape in raw format but the event headers are copied and stored in an Oracle DB. Event reconstruction requires about 700 ms per event in average. Using the CERN PC farm the reconstruction of all events from one year requires several months.

Detector alignment and calibration must be performed before the reconstruction. The alignment task is particularly delicate. More than 200 planes have to be aligned and at least 3 degrees of freedom must be tuned (the rotation in the detector plane, the translation along the coordinate measured by the plane and the translation along the beam). The alignment must be performed with an accuracy of a fraction of the detector resolution, which is better than 100 $\mu$m for many planes. In addition magnetic fringe field move the detectors or affect their measurements, which means that we must be able to perform the alignment with the field on [1].

We developed a tool which is described in COMPASS note 2003-04, added in the addendum. It is based on minimizing the sum of the $\chi^2$ of all tracks. This is possible, in spite of the very large number of parameters, due to some matrix manipulations [48]. The method was generalized to allow alignment with magnetic field on, but a special care should be taken not to introduce any bias on the momentum. The tool is working, it provides a reasonable alignment, much better than previously obtained with standard alignment methods based on correcting average residuals. However, it appears that, at the required level of accuracy, the pitches are not always nominal and sometimes not even constant over a detector plane. Studies are going on to cope with this difficulty in order to further improve the alignment.

---

[1]an alignment with field off remains needed in order to get a reference for momentum measurement.

# 4.3  The measurement of $\Delta g$

As discussed in section 2.5.2, $\Delta g$ can be measured with a polarized electromagnetic probe through the PGF process, $\gamma g \to q\bar{q}$. This process can be tagged by the production of either open charm or high $p_t$ hadron pairs. We will now discuss both channels in the framework of COMPASS.

## 4.3.1  Measurement of $\Delta g$ through open charm

The PGF can be tagged through $c \to D^0 \to K\pi$. Note that, due to the small branching ratio of about 4% for $D^0 \to K\pi$ and in order to keep a reasonable statistics, we will not tag both $c$ and $\bar{c}$ but only one of them. So we cannot reconstruct the PGF kinematics and determine the fraction, $x_g$, of the proton momentum carried by the gluon. The measured asymmetry will then be an average over a range in $x_g$, $A = \int \Delta\sigma \Delta g(x_g) / \int \sigma g(x_g)$. Note that, in the following, when we mention $D^0 \to K\pi$ we mean both $D^0 \to K^-\pi^+$ and $\overline{D}^0 \to K^+\pi^-$.

Due to multiple scattering, the $D^0$ has to be identified by its invariant mass. In these conditions there is an important *combinatorial* background of $K\pi$ pairs of all masses and the $D^0$'s appear as a peak in the $K\pi$ mass distribution. The $D^0$ signal will be integrated over a window around the peak. It is then very important to have a good resolution in the reconstructed $K\pi$ mass in order to have a narrow window and not to integrate too much background.

The $D^0$ have spin zero, so they decay isotropically in their rest frame. Their distribution in $\cos\theta^*$ is flat, where $\theta^*$ is the angle of the $K$ in the $D^0$ rest frame, whereas the distribution of the background is peaked around $|\cos\theta^*| = 1$. The background peaks at lower values of $z_D = E_D/\nu$ than the $D^0$ signal. In order to improve the $S/B$ ratio, the cuts $|\cos\theta^*| < 0.5$ and $z_D > 0.25$ are applied as illustrated in Fig. 4.3.

About 30% of the $D^0$ actually come from the decay of a $D^*$, i.e. $D^{*+} \to D^0\pi_s^+$ (and $D^{*-} \to \bar{D}^0\pi_s^-$). Tagging those $D^0$ with the additional soft pion, $\pi_s$, considerably reduces the background. The difference of mass $\Delta M = M_{D^*} - M_{D^0} = 145$ MeV is not much larger than the pion mass, 139.6 MeV. This leaves little energy available for the additional pion, which we call a soft pion, $\pi_s$. Due to this low momentum a moderate resolution on $\pi_s$ momentum is required to get a precise measurement of $\Delta M$. In addition, due to the small difference of mass there is little phase space available for background. In these conditions the kinematical cuts can be released to $|\cos\theta^*| < 0.85$ and $z_D > 0.2$.

In the COMPASS proposal the open charm muoproduction cross-section is evaluated starting from the measured photo-production cross-sections [49], multiplying by the virtual photon flux and a dipole form factor, $(1 + Q^2/M_0^2)^{-2}$, with $M_0 = 3.9$ GeV. This gives 1900 pb for a 100 GeV beam energy and a $0.35 < y < 0.85$ cut. With $2 \cdot 10^8$ muons per spill and a 120 cm long $^6$LiD target (see section 4.1), the luminosity is 43 pb$^{-1}$ per day and we expect 82,000 charm events per day.
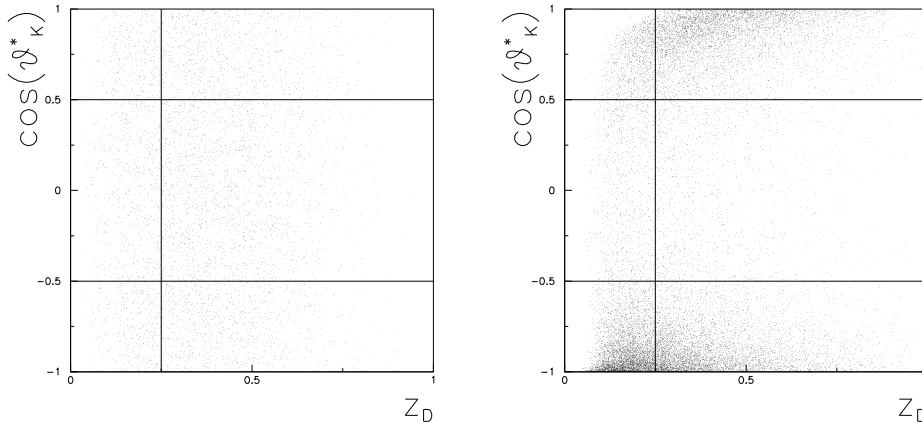
Figure 4.3: Distribution of $D^0$ signal (left) and combinatorial background (right) as a function of $\cos \theta^*$ and $z_D$. The lines indicate the kinematical cuts proposed.

In average 1.23 $D^0$ (or $\bar{D}^0$) are produced per charm event. Due to the $D^0 \to K\pi$ branching ratio of 0.04, about 4000 $D^0$ are expected per day. There are reduction factors due to kinematical cuts (0.5 for $\cos \theta^*$ and 0.71 for $z_D$), acceptance (0.84), re-interaction of the hadrons (0.76) which gives a final number of 877 $D^0$ per day. For the $D^*$ we have in average 0.60 $D^*$ per charm event, a branching ratio of 0.027 and we expect 295 $D^*$ per day. Assuming a 10 MeV resolution on the $D^0$ mass resolution $S/B$ ratio of 0.26 and 6.7 are expected for the $D^0$ and $D^*$ channels, respectively.

The statistical error on the asymmetry is

$$\delta A = \frac{1}{P_\mu P_t f D} \frac{\sqrt{1 + B/S}}{\sqrt{S}}. \tag{4.1}$$

Assuming 1.5 year of 150 days and an overall efficiency of 0.25 for the beam availability, the data taking and the reconstruction efficiency, this gives $\delta A = 0.076$ and 0.064 for the two channels. Combining them, taking into account that 20% of the $D^0$ sample is included in the $D^*$ sample, the proposal gives $\delta A = 0.051$ and $\delta(\Delta g/g) = 0.14$.

## $D^0$ mass resolution

We developed a special tool to compute the $D^0$ mass resolution. This is done analytically, event by event, as described in COMPASS note 2000-13, added in the addendum. For a given track we start from the detector resolutions and the distribution of materials and compute the covariance matrix $S$ of the measurements in the different planes, including the correlation between these measurements due to multiple scattering. The generalized $\chi^2$, which takes into account the correlations, is defined as

$$\chi^2 = \sum_{ij} \left[ x_i - F(z_i, \alpha) \right] (S^{-1})_{ij} \left[ x_j - F(z_j, \alpha) \right]. \tag{4.2}$$

The covariance matrix of the track parameters is computed using the standard matrix formulas [50]. Then error propagation techniques are applied to obtain the error on $M_{D^0}$ and $\Delta M$. The different contributions to the error can be computed independently: the error due to the momentum, the error due to the angle as measured by the spectrometer, the contribution of their covariance, and the error due to multiple scattering inside the target.

The full procedure is the following. The AROMA event generator [51] is used to produce a set of $D^0 \to K\pi$ events. The tracks are propagated through the SM1 field using a Runge Kutta method and the trajectories are stored in a ntuple. The set up, i.e. the positions and resolutions of the detectors and the distribution of materials, are defined in an input file. The mass resolution can be analytically computed event by event as described above. This last step requires on the order of 1 mn of a 300 MHz CPU for 10,000 events, after which another set-up can be studied. This tool proved to be extremely useful for the optimization of some parts of the spectrometer.

The first result was a determination of the average resolution, found to be on the order of 17 MeV. This showed that the 10 MeV $D^0$ mass resolution of the proposal was based on too naive assumptions. In particular, the amount of material in the target was underestimated. Fig 4.4 presents the mass resolution and the different contributions to it, as a function of the $D^0$ energy.
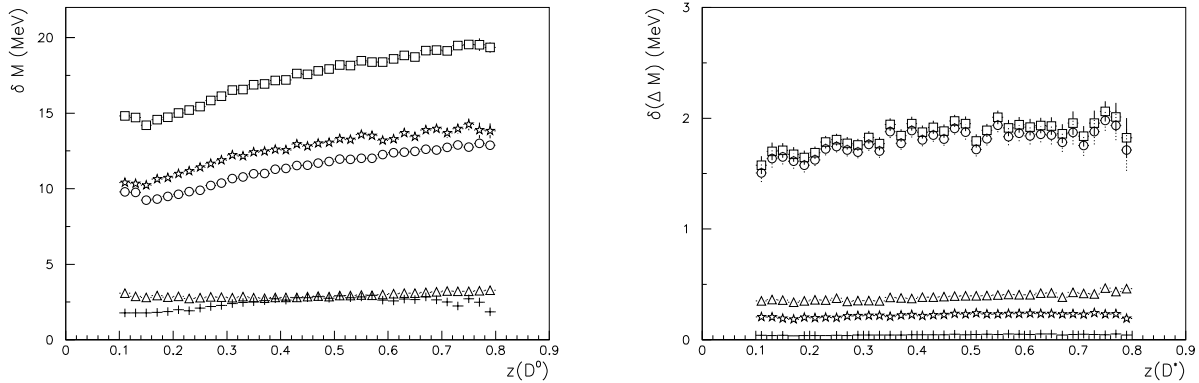


Figure 4.4: Left: Different contributions to the $D^0$ mass resolution as a function of $z_D$ for a beam energy of 160 GeV. From top to bottom, the total contribution (squares), the contribution from momentum (stars), the contribution from multiple scattering in target (circles), the contribution from angle as measured in the spectrometer (triangles) and the covariance term between the angle and the momentum (+). The covariance contribution is actually negative and we plot the square root of the absolute value of the contribution to $(\delta M)^2$. Right: same thing for the resolution in $M_{D^*} - M_{D^0}$. In this case the resolution is completely dominated by the multiple scattering in the target.

**Re-evaluation of the expected results**

At some point it appeared that the new large bore solenoid magnet which was foreseen for the polarized target would not be available in time. In addition only one straw station out of three was ready. We investigated what could be done in terms of the open charm channel with the old SMC solenoid magnet and the available straw station. This is detailed in COMPASS note 2002-2, added in the addendum.

A weighted method was used for the asymmetry extraction. As discussed in section 2.2.2 such a method was used previously in the SMC with a weight $w = fDP_\mu$. Here we generalize the method including $S/(S+B)$ in the weight and replacing the depolarization factor by the PGF analyzing power $a_{LL}$. In this case formula 3.5 directly provides $\Delta g/g$ instead of the asymmetry. Due to these additions, the variance of the weight is much larger than for SMC and the gain in statistics, equivalent in terms of number of events to a factor $\langle w^2 \rangle/\langle w \rangle^2 = 1 + \sigma_w^2/\langle w \rangle^2$, is also much larger. This factor gets particularly large for COMPASS because $w$ changes sign over the acceptance, due to $a_{LL}$. It reaches about 1.6.

In order to obtain the same open-charm cross-section as in the proposal the AROMA cross-section had to be multiplied by a so-called *K factor* of 1.7. The combinatorial background was simulated using PYTHIA 6.2 [52] and the $S/B$ ratio was tabulated as a function of $\cos\theta^*$ and $z_D$. The mass resolution was estimated with the procedure described above.

Different beam energies were studied. When the energy increases the charm cross-section increases faster than the background cross-section; the particles are boosted more forward and are more likely to enter the acceptance of the SMC PT magnet; the degradation of the mass resolution appears to be limited; and the reduction of $\langle a_{LL}^2 \rangle$ is also small. However, when going above 160 GeV one cannot any longer reach the nominal intensity, and at 190 GeV the intensity is reduced by 30%. The optimal is then a beam energy around 160 GeV.

We also showed that once the acceptance is reduced by the SMC PT magnet, most of the acceptance after SM1 can be covered by Saclay DCs. It was then decided to build one more DC station, to keep one DC station before SM1 and install 2 stations after SM2 together with the available straw station. Fig. 4.5 presents this reduced set up which was used for the 2002 and 2003 data taking.

Finally, we showed that the reduction in acceptance due to SMC magnet and the degradation of the $D^0$ mass resolution can be more than balanced by using the event weighting and going to 160 GeV.

## 4.3.2   Measurement of $\Delta g$ through high $p_t$ hadron pairs

As discussed in section 2.5.2, high $p_t$ hadron pairs select the Photon Gluon Fusion (PGF) processes but also a background of QCD Compton (QCDC) processes and in practice
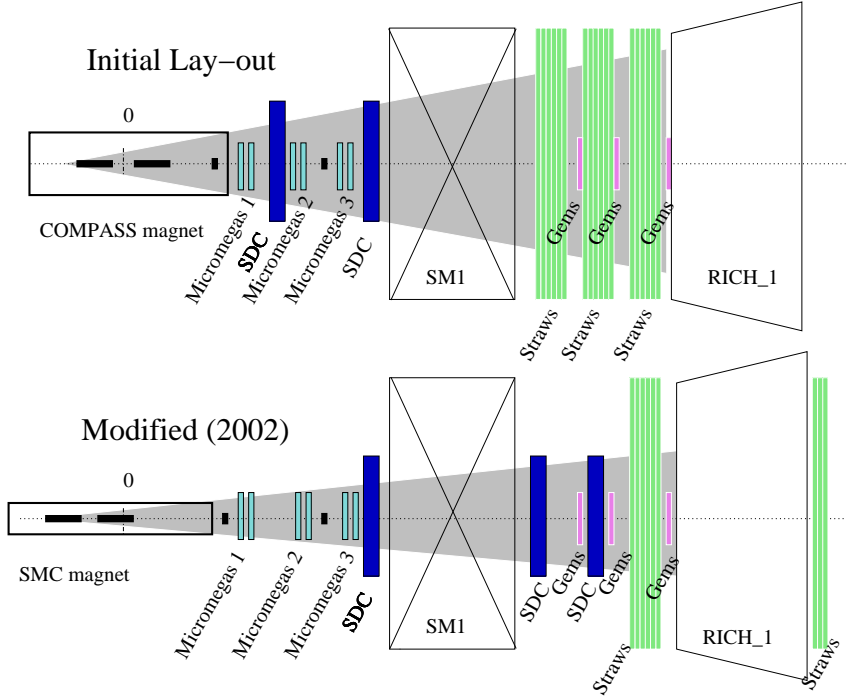
Figure 4.5: Reduced set up with the SMC PT magnet and DCs after SM1.

there is in addition some remaining Leading Order (LO) processes. The asymmetry in high $p_t$ hadron pair production can then be written as:

$$A^{lN \to h_1 h_2} = \langle \frac{\Delta g}{g} \rangle \langle a_{LL}^{PGF} \rangle R^{PGF} + \langle A_1 \rangle \langle a_{LL}^{QCDC} \rangle R^{QCDC} + \langle A_1 \rangle \langle a_{LL}^{LO} \rangle R^{LO} \qquad (4.3)$$

where the $\langle a_{LL} \rangle$ are the mean analyzing powers for the three processes; $R^{PGF}$, $R^{QCDC}$ and $R^{LO}$ are the fractions of the corresponding types of events. Since QCDC and LO correspond probe quarks inside the nucleon instead of $\Delta g/g$ they involve the $\Delta q/a$ weighted with the squared charge, i.e. the inclusive virtual photon asymmetry $A_1$. For LO processes, $a_{LL}$ is simply the depolarization factor $D$.

If we assume that the direction of the two high $p_t$ hadrons gives the direction of the $q$ and $\bar{q}$ of the PGF process, we can reconstruct the PGF kinematics. In particular we get $\hat{s} = \nu^2 \tan\theta_1 \tan\theta_2$, where $\theta_1$ and $\theta_2$ are the angles of the two hadrons in the laboratory frame relative to the virtual photon. This allows us to compute $x_g = (\hat{s} + Q^2)/2pq$.

The $A^{lN \to h_1 h_2}$ asymmetry will be measured and $A_1$ is experimentally known. But the $\langle a_{LL} \rangle$ and the ratios $R$ have to be obtained from simulations. The uncertainty in these quantities will probably be the dominant systematic error.

If the analysis is limited to $Q^2 > 1$ GeV$^2$ data, one can use a DIS event generator like LEPTO [53] to compute the required $a_{LL}$ and $R$. There is about 10 times more statistics if all $Q^2$ are used. In this case the PGF and the QCDC are well defined with a hard scale defined by e.g. $\sum p_t^2$; the other processes cannot really be called LO they are rather resolved
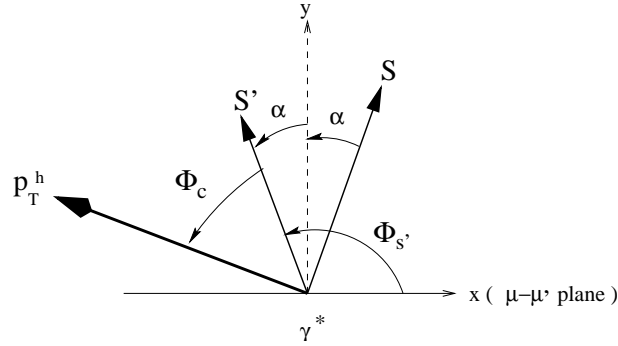
Figure 4.6: Definition of the Collins angle, $\phi_c = \phi_h - \phi_{S'}$, in the plane perpendicular to the virtual photon direction.

photon processes. This can only be simulated in a model dependent way, for instance with the PYTHIA event generator which uses the vector meson dominance model.

For the PGF when one of the high $p_t$ hadrons is a $K$, it is likely that the initial $q\bar{q}$ pair was a $s\bar{s}$ pair and then the second high $p_t$ hadron is likely to be also a $K$. Selecting $K^+K^-$ pairs at high $p_t$ provides therefore a sample with a larger fraction of PGF and then smaller systematic errors. Unfortunately, the number of events is reduced by an order of magnitude.

In contrast with the open charm channel, the high $p_t$ channel provides an estimate of $x_g$. In addition the statistics is much larger but the measurement is not as clean, and systematic errors arising from the estimate of $\langle a_{LL} \rangle$ and $R$ are likely to dominate statistical errors. The large statistics should, however, help in mastering the systematic errors since $\Delta g/g$ obtained in many different ways can be compared: the analysis can be limited to $Q^2 > 1$ GeV$^2$, or performed in some 10 bins in $Q^2$ with equivalent statistics; if all $Q^2$ are used there are enough data to split them in bins in $\sum p_t^2$ with different contributions of PGF, QCDC and LO; the special $K^+K^-$ sample provides another independent measurement; . . .

## 4.4   Transversity

COMPASS plans to run some 20% of the time in transverse spin mode. The three ways to access transversity with a lepton beam, introduced in section 2.4.1, will be used. Only the Collins effect was studied in details so far. It implies an azimuthal dependence of the event yield in terms of the *Collins angle* $\phi_c$. The Collins angle is the azimuthal angle (with respect to the virtual photon direction) between the final hadron and the final quark spin, $\phi_c = \phi_h - \phi_{S'}$, as illustrated in Fig. 4.6, where we define angles relative to the lepton scattering plane. The angle $\phi_{S'}$ is not directly measured but the absorption of the virtual photon results in $\phi_{S'} = \pi - \phi_S$, and the Collins angle can be expressed in terms of measured angles, $\phi_c = \phi_h + \phi_S - \pi$.
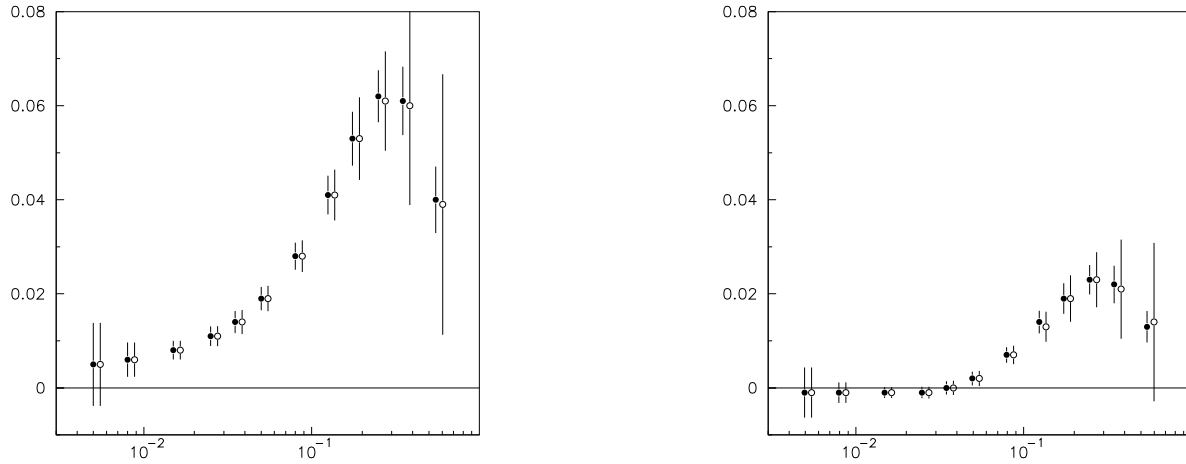
Figure 4.7: Expected error bars on $x \sum_q e_q^2 \Delta_T q(x)$ for proton (left) and deuteron (right) targets, both for the new large bore (full circle) and the old SMC (open circle) polarized target magnets.

The event yield is then $N = N_0 \left[1 \pm f P_T D_{nn} A_\phi \sin \phi_c\right]$, where $D_{nn} = (1-y)/(1-y+y^2/2)$ is the fraction of the initial quark transverse polarization which remains after the absorption of the virtual photon. The physical asymmetry can be expressed as $A_\phi = \left(\sum e_q^2 \Delta_T q(x) \Delta_T^0 D_q^h(z)\right)/\left(\sum e_q^2 q(x) D_q^h(z)\right)$ where $\Delta_T^0 D_q^h(z)$ is the polarized fragmentation function which tells how much of the quark transverse polarization is reflected in the hadron azimuthal asymmetry.

It should be stressed that the measurement of the Collins angle asymmetry provides the product $\Delta_T q(x) \times \Delta_T^0 D_q^h(z)$ and that $\Delta_T^0 D_q^h(z)$ is still unknown even if it is planned to be measured at Belle in $e^+ e^-$ collisions. A Collins angle analysis of the small sample of SMC transverse data was performed [54] and provided an asymmetry $A_\phi p \pi^+ = 0.11 \pm 0.06$, which is less than $2\,\sigma$ from zero. Hermes measured the azimuthal asymmetry for a target polarized parallel to the beam [55]. This implies a small contribution perpendicular to the virtual photon direction. It is proportional to $\sin \theta_\gamma$ and then to $1/Q$, so that it is of the same size as higher twist contributions. They measured $A_\phi^{p\pi^+} = 0.022 \pm 0.005 \pm 0.003$.

We simulated a measurement at COMPASS with a 160 GeV beam and the reduced acceptance due to the SMC polarized target magnet. The details can be found in Ref. [56] included in the addendum. We assumed $\Delta_T q = \Delta q$ and $\Delta_T^0 D_q^h(z)/D_q^h(z) = 0.75z$, which applied to the SMC and Hermes cases, gives smaller asymmetries than the ones they measured. Fig 4.7 presents the expected measurement for 30 days on proton (NH$_3$) and 30 days on deuteron ($^6$LiD). We see that a significant measurement can be performed with the new large bore PT magnet. At low $x$, where $W$ is large, hadrons have large momenta and are at small angles, they enter the SMC magnet acceptance and the measurement is as good as with the new magnet. At high $x$ however the measurement using the SMC magnet is problematic.

Hermes has recently shown first results [57] with a transversely polarized target. They seem to indicate that favored (e.g. $u \to \pi^+ = u\bar{d}$) and disfavored (e.g. $u \to \pi^- = \bar{u}d$) polarized fragmentation functions, $\Delta_T^0 D_q^h$, could be of opposite sign.

## 4.5  Other physics

In addition to $\Delta g$, several other channels of physics will be studied with a longitudinally polarized target. Due to a factor 5 in intensity and a factor 2 in dilution factor (equivalent to a factor 4 in terms of number of events) COMPASS will get much higher statistics than SMC for inclusive and semi-inclusive measurement. A more precise measurement of $g_1$ will be particularly relevant at low $x$ where the error bars blow up (see Fig. 3.9) due to the factor $x$ in the numerator of $g_1 = A_1 F_2/(2x(1 + R))$. This would allow for a more reliable low $x$ extrapolation of $g_1$ and a reduction of the dominant systematic error on $\Gamma_1$ and $a_0$. The semi-inclusive data will allow for a more accurate determination of the polarized pdf's. In particular the measurement of the asymmetry for production of $K^+$, $K^-$ and $K^0$ will provide a determination of the strange polarized pdf, $\Delta s(x)$. It will be possible to measure the $\Lambda$ polarization through the angular distribution of the decay $\pi$ and $p$. With a transversely polarized target the inclusive spin structure function $g_2$ will be measured in parallel with transversity measurements.

There is a complete set of measurements planned with $p$, $\pi$, $K$ and hyperon beams. The electromagnetic response of unstable particles, like $\pi$, $K$ and hyperons, will be studied by scattering them on the Coulomb field of a nuclear target and measuring the Primakov reaction, e.g. $\pi + p \to \pi + \gamma + p$. This provides the electric and magnetic polarisabilities of the beam particle. Central collisions of $p$ beam on $p$ target favor the production of glue-balls and exotic mesons and will be used to search for them. Semi-leptonic decays of charm hadrons will be used to study Heavy Quark Effective Theory (HQET) and a search for doubly charmed baryons can also be performed.

## 4.6  Status of the experiment

The commissioning of the spectrometer started in 2001 with part of the detectors. The full commissioning with all detectors was done in 2002 and followed by the first period of physics data taking. Data taking went on in 2003 but with poor beam efficiency. In addition, the number of days of data taking allocated to the experiment each year is lower than assumed in the proposal. The SPS will not run in 2005 and discussions are ongoing for a phase II of COMPASS starting in 2006.

A first measurement of the double spin asymmetry in the high $p_t$ channel out of the 2002 data without $Q^2$ cut was however obtained [58]:

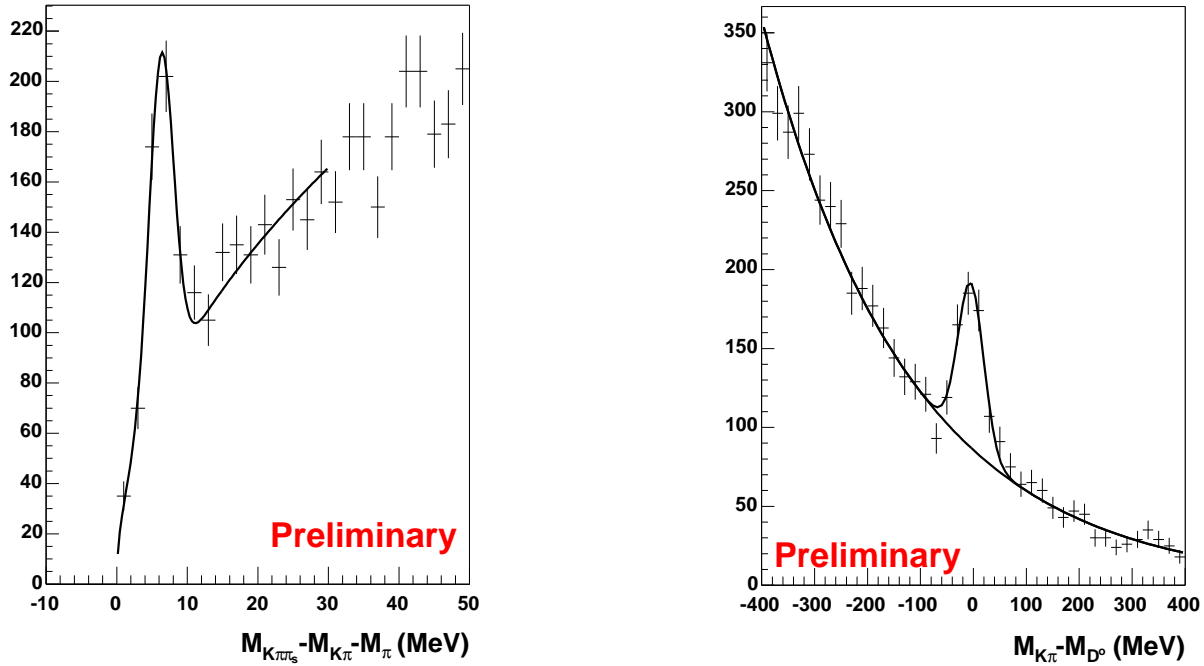$$\frac{A_{LL}^{\mu d \to hh}}{D} = -0.065 \pm 0.036 \pm 0.010. \tag{4.4}$$

Figure 4.8: $D^* \to D^0\pi \to K\pi\pi$ observed signal with the reconstructed $\Delta M$ for events such that $|M_{K\pi} - M_{D^0}| < 30$ MeV on the left, and $M_{K\pi}$ for events such that $m_\pi + 3.1 < \Delta M < m_\pi + 9.1$ MeV on the right.

Assuming a fraction of PGF events on the order of 1/4, this will provide a statistical error on $\Delta g/g$ of 0.17. MC studies are going on to evaluate more precisely the ratio of PGF events and the asymmetry of the background. Given that the PGF analyzing power $\langle a_{LL}^{PGF} \rangle$ is negative, the measured negative asymmetry is a hint that $\Delta g/g$ should be positive. Projections for the period 2002-2004 give a statistical error on $\Delta g/g$ on the order of or better than 5%, which will allow for several bins in $x_g$. If we limit the analysis to $Q^2 > 1$, where the background is easier to take into account as discussed in section 2.5.2, we loose a factor 10 in statistics but still get an accuracy on the order of 0.16.

Fig. 4.8 shows the first $D^* \to D^0\pi \to K\pi\pi$ signal obtained from 2002 data. The width of the reconstructed $D^0$ mass is $26 \pm 3$ MeV. The signal to background ratio is on the order of 1. This is not as good as in the proposal due to the degradation of the mass resolution and to a still very preliminary RICH analysis which does not provide yet a very pure $K$ sample. In addition the number of events is lower than expected in the proposal. In these conditions we cannot yet obtain a measurement of $\Delta g/g$. The 2003 data are however already quite better and the problem has been studied in details [59]: a complete analysis of all sources of loss has been performed and they are now understood; possibilities of recovery from these losses have been evaluated and several additional gains, to be provided by a more refined analysis of the data than assumed in the proposal, have been demonstrated. Combining all these factors a statistical error on the order of 0.24 is expected from the open charm channel out of the 2002-2004 data.

# 4.7   Competing experiments

The Relativistic Heavy Ion Collider (RHIC) in Brookhaven will operate part of the time as a polarized proton-proton collider, with a luminosity $\mathcal{L} \approx 2 \times 10^{32}$. The STAR and PHENIX experiments will use this time to study gluon polarization and transversity [60]. The asymmetry in the production of $\vec{p}\vec{p} \rightarrow \gamma+$ jet $+X$ events will be used to measure gluon polarization as discussed in section 2.5.3. In RHIC kinematics the background contribution from $q\bar{q} \rightarrow \gamma g$ events is small, on the order of 10%. A large range of $x_g$ will be covered, $0.01 \leq x_g \leq 0.3$ with a good statistical accuracy. The final accuracy will probably be limited by systematic errors due to background subtraction and deconvolution of $\Delta g \otimes \Delta q$.

Polarized quark distribution can also be measured with a good accuracy at RHIC. This will be done through parity violating $W$ production in $\vec{p}p$ collisions with the advantage of being independent of any fragmentation function.

The measurement of transversity through the Drell-Yan process will not be possible before a luminosity upgrade and for the moment RHIC will measure transversity through the distribution of pions in particular using the Collins effect.

There is also a proposal at SLAC [61] for the measurement of $\Delta g/g$ through open charm photo-production asymmetry. Charm events will be signed by a single large $p_t$ muon. This proposal is frozen due to financial constraints.

# Chapter 5

# Conclusions

This spin of the nucleon can be decomposed in the contributions of its partonic constituents :

$$\frac{1}{2} = \frac{1}{2}\Delta\Sigma + \Delta g + L_q + L_g. \tag{5.1}$$

Inclusive polarized DIS experiments at CERN, SLAC and DESY measured the axial matrix element of the nucleon $a_0$ and found it small, $a_0 \approx 0.2$. Naively $a_0 = \Delta\Sigma$ but actually, due to the axial anomaly, $a_0 = \Delta\Sigma + n_f\frac{\alpha_s}{2\pi}\Delta g$.

A strong interest in the measurement of $\Delta g$ now exists in the community. Measurements of $\Delta g(x)$ will be performed in the coming years at RHIC and CERN (COMPASS) and may be at SLAC. Furthermore, RHIC and COMPASS will perform several measurements using different channels. So we will get many measurements with completely different sources of systematic errors, both from the experimental point of view and, more important, from the point of view of the interpretation. In the longer term our knowledge of $\Delta g$ might be further improved by measurements with a proposed polarized electron beam colliding RHIC proton beam [62]. In particular this would provide us with a measurement of $g_1$ at large $Q^2$ and allow for a QCD analysis resulting in an accurate first moment, $\Delta g = \int_0^1 \Delta g(x)dx$. This would also allow for an accurate measurement of $g_1$ down to $x = 10^{-4}$, dramatically reducing the error due to low $x$ extrapolation, which is the dominant error on the first moment, $\Gamma_1 = \int_0^1 g_1(x)dx$, and on $a_0$.

Our knowledge of the different flavors of polarized quark distribution functions, in particular the strange one, will be greatly improved by semi-inclusive measurements at COMPASS and measurements of the parity violating asymmetry in $W$ production at RHIC.

Concerning transversity first results have just been shown by Hermes and more results will appear soon from Compass and RHIC using the Collins effect. This will be combined with a measurement of the analyzing power at Belle. After an increase of the luminosity RHIC should also provide a measurement through Drell-Yan, which will be independent of any analyzing power.

The last two terms of the nucleon spin puzzle, Eq 5.1, are very difficult to attack. There

is however a connection of $L_q$ with the generalized parton distributions (GPD) through the Ji sum rule. These GPDs can be measured through exclusive processes like deep virtual Compton scattering, $\gamma^* p \to \gamma p$, or hard exclusive vector meson production, $\gamma^* p \to V p$ [63]. Preliminary measurements in this direction are going on at JLab and DESY. The possibility of measurements with a modified COMPASS setup is being studied.

# Bibliography

[1] Nathan Isgur in "The Spin Structure of Nucleon", edited by B. Frois, V.W. Hughes and N. de Groot, World Scientific, Singapore, 1997

[2] J. Ashman et al., EMC coll., Phys. Lett. **B206** (1988) 364, Nucl. Phys. **B328** (1989) 1

[3] http://www.slac.stanford.edu/library/topcites/

[4] For unpolarized DIS, G. Altarelli, Phys. Rep. 81 (1982) 1.
For polarized DIS, M. Anselmino, A. Efremov and E. Leader, Phys. Rep. 261 (1995) 1, hep-ph/9501369; B. Lampe and E. Reya, Phys. Rep. 332 (2000) 1, hep-ph/9810270

[5] F. Halzen and A. D. Martin, *Quarks and Leptons*, (Wiley, New York, 1984).
F.E. Close, An introduction to Quarks and Partons, Academic Press, 1979.
E. Leader, Spin in particle physics, Cambridge Univ. Press, 2001.

[6] W. Greiner and A. Schaeffer, Quantum Chromodynamics, Springer.

[7] D. Adams et al., Phys. Rev. D56 (1997) 5330.

[8] M. Breidenbach et al., Phys. Rev. Lett. **23** (1969) 935.

[9] G. Altarelli and G. Parisi, Nucl. Phys. **B126** (1977) 298.
V. N. Gribov and L. N. Lipatov, Sov. J. Nucl. Phys. **15** (1972) 438.
Y. L. Dokshitzer, Sov. Phys. JETP **46** (1977) 461.

[10] S.Chekanov et al., ZEUS cool., Eur. Phys. J. **C21** (2001) 443.

[11] A. Benvenuti et al., BCDMS coll., Phys. Lett. **B223** (1989) 485.

[12] M. Arneodo et al., NMC coll., Nucl. Phys. **B483** (1997) 3.

[13] M.R. Adams et al., E665 coll., Phys. Rev. **D54** (1996) 3006.

[14] A. V. Manohar, lecture at the Lake Louise Winter Institute, 1992, hep-ph/9204208.

[15] The SMC, Phys. Rev. **D60**, 072004 (1999); Erratum ibid. **D62** (2000) 079902.

[16] L. N. Hand, Phys. Rev. **129** (1963) 1834.

[17] J. Soffer and O. V. Teryaev, Phys. Lett. B 490 (2000) 106.

[18] J. Kodaira, S. Matsuda, K. Sasaki, and T. Uematsu, Nucl. Phys. **B159** (1979) 99; J. Kodaira, S. Matsuda, T. Muta, and T. Uematsu, Phys. Rev. **D20** (1979) 627.

[19] R. Mertig and W. L. van Neerven, Z. Phys. **C70** (1996) 637. W. Vogelsang, Phys. Rev. **D54** (1996) 2023.

[20] J. D. Bjorken, Phys. Rev. **148** (1966) 1467. Phys. Rev. **D1** (1970) 1376.

[21] J. Ellis and R. L. Jaffe, Phys. Rev. **D9** (1974) 1444; Phys. Rev. **D10** (1974) 1669.

[22] SMC, D. Adams et al., Phys. Rev. **D58** (1998) 112001.

[23] SMC, D. Adams et al., Phys. Rev. **D58** (1998) 112002.

[24] E142, Anthony et al. Phys. Rev. **D54** (96) 6620; E143, Abe et al., Phys. Rev. **D58** (98) 112003. E154, Abe et al. Phys. Lett. **B405** (97) 180; E155, Anthony et al. Phys. Lett. **B493** (00) 19, Phys. Lett. B463 (1999) 339.

[25] HERMES, A. Airapetian et al., Phys. Lett. **B442** (1998) 484.

[26] G. Altarelli and G. G. Ross Phys. Lett. **B212** (1988) 391. R. D. Carlitz, J. C. Collins, and A. H. Mueller Phys. Lett. **B214** (1988) 229.

[27] S. I. Adler, Phys. Rev. **177**(1969) 2426; J. S. Bell and R. Jackiw, Nuovo cimento **51A** (1969) 47.

[28] R. D. Ball, S. Forte and G. Ridolfi, Phys. Lett. B **378** (1996) 255

[29] R. Mertig, W.L. Van Neerven, Z. Phys. C 70 (1996) 637. W. Vogelsang, Phys. Rev. D 54 (1996) 1517.

[30] J. Ralston and D.E. Soper, Nucl. Phys. **B152**, 109 (1979).

[31] X. Artru and M. Mekhfi, Z. Phys. **C45** (1990) 669.

[32] V. Barone, A. Drago and P.G. Ratcliffe, Phys. Rep. **359** (2002) 1 or hep-ph/0104283.

[33] J.C. Collins, Nucl. Phys. B396 (1993) 161.

[34] A. Bravar, D.v. Harrach and A. Kotzinian, Phys. Lett. **B421** (98) 349. hep-ph/9710266.

[35] Nucl. Instr. Meth. **A 437** (1999) 23.

[36] A. Abragam and M. Goldman, Rep. Prog.Phys. **41** (1978) 395.

[37] J.M. Le Goff et al., Nucl. Instr. Meth. **A356** (1995) 96.

[38] Y. Kisselev et al., Zh. Eksp. Teor. Fiz. 94 (2), 344 (1988); Sov. Phys. JETP **67**, 413 (1988).

[39] N. Doble et al., Nucl. Instr. Meth. **A343** (1994) 351.

[40] SMC, Nucl. Instr. Meth. **A 343** (1994) 363.

[41] SMC, Nucl. Instr. Meth. **A 443** (2000) 1.

[42] A.A. Akhundov *et al.*, Fortsch. Phys. **44**, 373 (1996); A.A. Akhundov *et al.*, Sov. J. Nucl. Phys. **26**, 660 (1977); **44**, 988 (1986); JINR-Dubna Preprints E2–10147 (1976), E2–10205 (1976), E2–86–104 (1986); D. Bardin and N. Shumeiko, Sov. J .Nucl. Phys. **29**, 499 (1979).

[43] T.V. Kukhto and N.M. Shumeiko, Nucl. Phys. **B219**, 412 (1983); I.V. Akushevich and N.M. Shumeiko, J. Phys. **G20**, 513 (1994).

[44] SMC, Phys. Lett. B420 (1998) 180.

[45] COMPASS, G. baum et al., CERN-SPSLC-96-14,
`http://www.compass.cern.ch/compass/proposal`

[46] C. Bernet et al., to be published in Nucl. Instr. Meth.

[47] Y. Giomataris, Ph. Rebourgeard, J.P. Robert and G. Charpak, Nucl. Instr. Meth. **A376** (1996) 29.

[48] V. Blobel and C. Kleinwort, Conference on Advanced Statistical Techniques in Particle Physics, Durham, 18-22 March 2002, `www.desy.de/~blobel/pmille.ps` and `www.desy.de/~blobel/wwwmille.html`

[49] NA14, M.P. Alvarez et al., Z. Physics **C60** (1993) 53, and reference therein.

[50] Particle data group, Eur. Phys. Jour. **C15** (2000) 1.

[51] G. Ingelman, J. Rathsman and G. Schuler, Comp. Phys. Com **101** (1997) 135,
`http://www3.tsl.uu.se/thep/MC/`

[52] T. Sjöstrand et al., Comp. Phys. Com **135** (2001) 238;
`http://www.thep.lu.se/~torbjorn/Pythia.html`

[53] G. Ingelman, A. Edin and J. Rathsman, Comp. Phys. Com bf 101 (1997) 108,
`http://www3.tsl.uu.se/thep/MC/`

[54] A. Bravar (SMC Collab.), Nucl. Phys. Proc. Suppl. 79 (1999) 520.

[55] Hermes, Phys. Rev. Lett. 84 (2000) 4047

[56] J.M. Le Goff, Nucl. Phys. **A711** (2002) 56c.

[57] A. Airapetian et al, hep-ex/0408013, submitted to Phys. Rev. Lett.

[58] C. Bernet, PhD thesis, May 2004, université Paris sud Orsay.

[59] J.M. Le Goff et al., COMPASS note 2004-2

[60] G. Bunce et al., Ann. Rev. Nucl. Part. Sci. **50** (2000) 525; hep-ph/0007218.

[61] http://www.slac.stanford.edu/exp/e161/

[62] http://www.phenix.bnl.gov/WWW/publish/abhay/Home_of_EIC/

[63] M. Diehl, Phys. Rep. **388** (2003) 41 or hep-ph/0307382.